metals

MDPI

Article

Radiation Effects in Amorphous Metallic Alloys as Revealed by Mössbauer Spectrometry: Part II. Ion Irradiation

Marcel B. Miglierini [1,2]

[1] Institute of Nuclear and Physical Engineering, Faculty of Electrical Engineering and Information Technology, Slovak University of Technology, Ilkovičova 3, 812 19 Bratislava, Slovakia; marcel.miglierini@stuba.sk
[2] Department of Nuclear Reactors, Faculty of Nuclear Sciences and Physical Engineering, Czech Technical University, V Holešovičkách 2, 180 00 Prague, Czech Republic

Abstract: Due to their excellent magnetic properties, amorphous metallic alloys (AMAs) are considered for the construction of magnetic cores of radio-frequency cavities in accelerators. Here, they might be exposed to ion bombardment. The influence of irradiation by both light and heavy ions featuring low and high energies, respectively, is followed by the techniques of ^{57}Fe Mössbauer spectrometry. Modifications of surface layers in selected Fe-containing AMAs after ion irradiation are unveiled by detection of conversion electrons and photons of characteristic radiation whereas those in their bulk are derived from standard transmission spectra. Rearrangement of microstructure which favors the formation of magnetically active regions, is observed in surface regions bombarded by light ions. Heavy ions caused pronounced effects in the orientation of net magnetization of the irradiated samples. No measurable impact upon short-range order arrangement was observed. Part I of this paper is devoted to radiation effects in Fe-based AMAs induced by neutron irradiation.

Keywords: Mössbauer spectrometry; amorphous metallic alloys; structural modifications; ion irradiation; hyperfine interactions; short-range order

Citation: Miglierini, M.B. Radiation Effects in Amorphous Metallic Alloys as Revealed by Mössbauer Spectrometry: Part II. Ion Irradiation. *Metals* **2021**, *11*, 1309. https://doi.org/10.3390/met11081309

Academic Editor: Giovanni Principi

Received: 19 July 2021
Accepted: 16 August 2021
Published: 18 August 2021

1. Introduction

The ability to design, construct, and predict the properties of new materials, which are expected to be used in extreme environments of increased radiation exposure, currently challenges research groups worldwide. Here, amorphous metallic alloys (AMAs) occupy a unique position because of their advantageous soft magnetic behavior. Thus, continuous specific research is needed to describe their characteristic physical properties in order to better understand the basic mechanisms involved in radiation processes.

AMAs are considered for use in nuclear facilities. However, using them in high-power high-energy accelerators brings an additional problem of their possible radiation damage. During the machine operation, all construction materials are exposed to irradiation by lost beam particles. The primary beam particles may interact with the material of the beam-pipe walls and produce secondary particles like light fragments and neutrons. At high beam intensities, even low-level beam losses may cause significant radiation load.

Recently, Fe-based soft magnetic AMAs were suggested as candidates for magnetic cores of accelerator RF-cavities to improve their performance [1–3]. In this particular application, they are exposed to ion irradiation that might affect their microstructure and magnetic properties [4–10]. The ion-induced radiation damage is due to displacement of target atoms by elastic and/or inelastic collisions. While the former dominate at low ion energies (a few tens of keV to a few MeV), the latter prevail at high ion energies (a few tens of MeV and higher), the corresponding ions being referred to as swift heavy ions [11].

Because of a disordered structure, AMAs were considered to be resistant against swift heavy-ion irradiation, however, changes of some of their macroscopic properties were recently reported [12–15] showing a continuing interest in these phenomena. Their importance is underlined also by the use of sophisticated experimental techniques based

on synchrotron radiation. Rodriquez et al. [16] successfully determined the radius of the tracks formed by swift heavy ions in various Fe-B-based AMAs using a small angle X-ray scattering technique. The use of synchrotron X-ray diffraction [17–19] and the so-called nuclear forward scattering of synchrotron radiation [20] have proved to be useful tools for investigation of radiation-induced dynamic transformations in AMAs by employing in situ high-temperature experiments in real time.

Nevertheless, in order to understand structural modifications that are taking place on an atomic level, suitable local-probe techniques should be introduced. Indeed, the pioneering work of Kuzmann and Spirov [21] highlights the application of Mössbauer spectrometry in the examination of amorphous alloys irradiated with energetic heavy ions. In addition, it also provides a short review on the use of different techniques in the study of radiation damage caused to different materials. Nevertheless, Mössbauer spectrometry turned out to be extremely important for revealing irradiation-induced modifications in the short-range order (SRO) of various types of AMA after swift heavy ion irradiation [22–30].

For example, Juraszek et al. [23] observed changes in the magnetic texture of $Fe_{81}B_{13.5}Si_{3.5}C_2$ alloys by ^{57}Fe transmission and conversion electron Mössbauer spectroscopy (CEMS) after the irradiation with swift Pb ions. The importance of CEMS in the investigation of the surfaces of ion-irradiated MGs was pointed out by Stichleutner et al. [28] who investigated Sn-Co-Fe and Sn-Ni-Fe amorphous thin films after irradiation with 246 MeV Kr and 600 MeV Xe ions, respectively. Modifications of SRO were reported using both ^{57}Fe and ^{119}Sn resonant nuclei.

It is noteworthy that studies of irradiation effects caused by low- and medium-energy ions upon classical compositions of AMAs are also reported and recently attracted the interest of several research groups [8,9,31–35]. Nonetheless, Mössbauer effect studies in this field are not so abundant [36–39] and it is not surprising that they emphasise the importance of surface modifications which are unveiled by the help of the CEMS technique. Eventually, conversion X-ray Mössbauer spectrometry (CXMS), which scans deeper surface regions than the CEMS technique, is also applied [38].

Accounting for the short overview of the impact of irradiation by ions upon structural (and magnetic) modifications of Fe-based AMAs, it seems that it is inevitable to study them on an atomic level with a suitable local probe method. Here, we will demonstrate that ^{57}Fe Mössbauer spectrometry meets these requirements. We will discuss its feasibility using selected examples of AMAs that were exposed to irradiation with both light and heavy ions featuring different energies. We will show that changes in hyperfine interactions between the nucleus and the electron shell are governed by rearrangement of the constituent atoms, including clustering and formation of stress centers caused by irradiation. They depend on the composition of the investigated samples as well as the nature of the bombarded particles. Radiation effects of neutrons, which represent a specific class of particle, were discussed in Part I of this paper [40].

2. Materials and Methods

2.1. Mössbauer Spectrometry

Mössbauer spectroscopy (MS) belongs to a few techniques that are able to scan local atomic arrangement of the investigated materials through hyperfine interactions between the nucleus and the electron shell of the resonant atoms [41]. A brief description of the most commonly used technique—^{57}Fe experiments in transmission geometry—was provided in Part I of this paper [40]. Differences between Mössbauer spectra of crystalline and amorphous materials were also explained and so were the variations in the spectra belonging to non-magnetic and magnetic samples. More detailed explanations can be found also elsewhere [42,43].

MS experiments performed in transmission geometry enable inspection of the entire volume of the investigated sample. In addition, two surface sensitive MS techniques can be applied. They are the so-called Conversion Electron Mössbauer Spectrometry (CEMS) and Conversion X-ray Mössbauer Spectrometry (CXMS) which provide information from subsurface regions down to the depth of ~200 nm and ~5 μm, respectively. They are especially suited for investigation of surface properties [44] including ion-irradiation induced radiation damage that is usually located in near surface regions [36–39]. In this way, it is possible to acquire complex information from both the whole sample's interior and/or its surface.

Standard Mössbauer spectrometer equipped with a ^{57}Co/Rh radioactive source moving with constant acceleration was employed to acquire experimental spectra at room temperature in transmission geometry, CEMS, and CXMS. We have used a 12.5 μm thick α-Fe foil to calibrate the velocity scale. Isomer shift values are given with respect to a room temperature Mössbauer spectrum of this foil. Mössbauer absorbers were prepared by covering approximately 1.5 cm^2 area by 1–1.5 cm long ribbons of the investigated AMAs.

Evaluation of Mössbauer spectra of ion irradiated samples was accomplished by the CONFIT software, version 5.2.35.1 [45]. Distributions of hyperfine magnetic fields, $P(B)$, and quadrupole splitting, $P(\Delta)$, were constructed by means of the appropriate number of partial sextets and doublets of Lorentzian lines, respectively, that were convoluted by a set of Gaussian distributions. Linewidth of the basic sextet and/or doublet was fixed to a value obtained from the corresponding calibration (typically ~0.26 mm/s). The following spectral parameters were refined: isomer shift, quadrupole splitting/shift, hyperfine magnetic field, relative area of the spectral component, widths of Gaussian distribution, and in case of the sextet its relative line intensities (areas).

2.2. Investigated Materials and Irradiation Conditions

Effects of ion irradiation were studied upon Fe-based AMAs by applying ^{57}Fe Mössbauer spectrometry for their microstructural characterization. Namely, the use of this local-probe method has determined the choice of appropriate chemical compositions featuring a sufficiently high content of iron. An underlying criterion took into consideration such AMAs that, eventually, can be used as precursors for the preparation of the so-called nanocrystalline alloys. Namely, NANOPERM- [46] and FINEMET-type [47] AMAs were considered due to their suitable magnetic properties. Finally, having some experience with the effects of neutron irradiation upon Fe-based AMAs [48], we have chosen such compositions that are especially sensitive to even tiny structural modifications as for example the Fe-Mo-Cu-B-type AMA [49]. This system exhibits close-to-room magnetic ordering temperature at ambient conditions. Thus, it is prone to changes of its magnetic microstructure caused by external factors—ion irradiation—due to short-range order rearrangement of the resonant atoms.

Accounting for their advantageous soft magnetic properties, some compositions comprising FINEMET-type AMAs are considered for practical applications in the construction of magnetic resonance cavities of accelerator structures [1–3]. To understand the possible degradation of magnetic parameters and the effects of ion bombardment upon probable deterioration of their performance parameters, their response to such radiation damage should be known. Therefore, this was a strong motivation for choosing also this type of AMA for our studies.

A summary of the investigated samples, which were in a form of ribbons, is provided in Table 1 together with their geometrical characteristics. Fe-Mo-Cu-B-type AMAs were prepared by the method of planar flow casting at the Institute of Physics, Slovak Academy of Sciences in Bratislava (courtesy of P. Švec and D. Janičkovič) while FINEMET, and VITROPERM® 800 are of commercial origin (Vacuumschmelze GmbH & Co KG, Hanau, Germany). It is noteworthy that some AMAs were produced from iron enriched to about 50% by the ^{57}Fe isotope and that is why their ribbon width is so small. Nevertheless, the state-of-the-art production has provided high-quality ribbons that facilitated, in particular,

the use of CEMS and CXMS techniques which are rather time consuming when samples with natural content of resonant ^{57}Fe nuclei (~2%) are measured. On the other hand, samples with enhanced content of ^{57}Fe are not suitable for transmission Mössbauer effect experiments due to their high effective thickness which causes significant broadening of absorption spectral lines. Consequently, these AMAs were inspected only by CEMS and/or CXMS techniques.

Table 1. Amorphous metallic alloys for ion irradiation experiments.

Composition	Sample's Label	Thickness (μm)	Width (mm)
$Fe_{76}Mo_8Cu_1B_{15}$	NANOPERM	~20	6
$^{57}Fe_{75}Mo_8Cu_1B_{16}$	Fe75	~20	1–2
$^{57}Fe_{81}Mo_8Cu_1B_{10}$	Fe81	~20	1–2
$Fe_{74}Cu_1Nb_3Si_{16}B_6$	FINEMET	22	20
[(1)] $Fe_{73}Cu_1Nb_3Si_{16}B_7$	VP 800	23	20

[(1)] VITROPERM® 800.

Ion irradiation of ribbon-shaped AMAs was performed in such way that the incoming ions were directed towards the shiny side of the ribbons. During preparation of amorphous ribbons by the process of rapid quenching, this side was exposed to the surrounding atmosphere (air). That is why it is also referred to as the air side while the opposite one, which was in direct contact with the quenching wheel, is dull and also called the wheel side. Due to the production process, both sides of the ribbon exhibit notable differences in surface morphology [50], the air side being more uniform and smooth. That is why it was chosen to face the ion beam. In order to ensure appropriate thermal contact with the irradiation base and, thus, to warrant that the ribbons will be not overheated during ion bombardment, pieces of the ribbons were firmly attached to a cooled sample holder. Failure to follow this condition might lead to irradiation-induced enhanced thermal load with a consequent crystallization of originally amorphous ribbons [38].

Ion irradiation was performed by low-energy (up to 130 keV) light ions (H, N) and swift heavy ions (^{131}Xe, ^{197}Au, ^{238}U) featuring very high energies (up to ~2 GeV). The former experiments were carried out at a cascade accelerator of the Slovak University of Technology [51] while ion beams with up to 11.1 MeV/u were used at the UNILAC accelerator at GSI Helmholtzzentrum für Schwerionenforschung Darmstadt [52]. Total fluences of up to 2.5×10^{17} ion/cm^2 and 10^{13} ion/cm^2 were reached for light and heavy ions, respectively. In particular, the irradiation with low energetic (and light) ions were preceded by SRIM2008 simulations to estimate the ion penetration range and radiation damage. The simulations were performed in a "full cascade" mode with the aid of the SRIM supporting software [53].

The depth-profiles of ionization (electronic stopping) and vacancy concentration were simulated. The latter was converted to DPA (displacement per atom). Table 2 presents parameters of the ion irradiation experiments. Results of simulations as collected from the original publications (see the column reference) are also included. They comprise characteristics of ion penetration curves like the depth at which the highest concentration of the stopped ions is found (maximum of ion range), the mean projected range, and the range straggling. In addition, the maximum of radiation damage (maximum of DPA) is also provided. This highest number of vacancies correlates well with the mean projected range of primary ions. Taking into consideration the presented data, the particular Mössbauer effect technique was chosen for characterization of the impact of ion irradiation, namely transmission geometry and/or CEMS/CXMS, in order to concentrate on the appropriate parts of ion-irradiated ribbons.

Table 2. Parameters of ion irradiation experiments.

Sample	Ion Parameters						
	Type	Energy (MeV)	Maximum of Ion Range (μm)	Mean Projected Range (μm)	Range Straggling (μm)	Maximum of DPA (μm)	References
$Fe_{76}Mo_8Cu_1B_{15}$	H	0.080	0.438	0.401	0.077	0.384	[37,54]
	N	0.130	0.180	0.148	0.051	0.123	[37,54]
$^{57}Fe_{75}Mo_8Cu_1B_{16}$	N	0.130	0.180	0.148	0.051	0.130	[38]
$^{57}Fe_{81}Mo_8Cu_1B_{10}$	N	0.130	0.180	0.148	0.051	0.123	[39]
$Fe_{74}Cu_1Nb_3Si_{16}B_6$	H	0.037	0.240	0.220	0.057	0.200	[37]
	N	0.110	0.153	0.133	0.047	0.114	[5,36]
	Au	593	19.3	18.9	0.575	18.9	[5,36]
	Xe	1450	>23			>23	[4,19]
$Fe_{73}Cu_1Nb_3Si_{16}B_7$	Au	2187	>23			>23	[17,52]
	U	1404	>23			>23	[18,52]

3. Results

Ion irradiation is fundamentally different from neutron irradiation due to the electric charge that ions have. The interaction mechanism with the irradiated material involves also excitation and ionization of the constituent atoms through which part of the ions' original energy is lost. Due to this, the incoming ions can travel within the given material, AMAs in our case, only a well-defined distance which depends upon their type and energy. Consequently, the effects of ion irradiation should be assessed taking these two parameters into account. Thus, in the following we will consider two cases:

1. Light ions accelerated to rather low energies;
2. Swift heavy ions.

Radiation effects of light ions will be demonstrated using two types of AMA that differ one from another namely in their dominating hyperfine interactions between the nucleus and the electron shell. While Fe-Mo-Cu-B-type alloys, namely NANOPERM, Fe75, and Fe81 (Table 1), exhibit under ambient conditions comparable electric quadrupole and magnetic dipole interactions that lead to close-to-room Curie temperature, FINEMET and VP 800 samples are highly magnetic. The former composition is thus very sensitive to any structural modification caused for example by radiation effects [40].

The experimental conditions for ion irradiation are listed in Table 2 comprising the investigated materials as well as irradiation ions and their energies. Within the first group of ions, H^+, i.e., protons, and N^+ ions are considered. Heavy ions are represented by ^{131}Xe, ^{197}Au, and ^{238}U. They were accelerated to the energies of up to 11.1 MeV/u which, for example, represents the total energy of more than 2 GeV for Au ions.

3.1. Light Ions

3.1.1. NANOPERM-Type $Fe_{76}Mo_8Cu_1B_{15}$ Amorphous Metallic Alloy

Radiation effects were studied after bombardment by 80 keV H^+ and 130 keV N^+ ions. Even though N^+ ions have higher energy, because of their considerably higher mass, maximum ion penetration range distribution was found at about 180 nm whereas the majority of lighter protons, although with smaller energy, have stopped at about 440 nm (see Table 2).

Selected examples of Mössbauer spectra recorded in transmission geometry, TMS, and by the CEMS technique are shown in Figure 1. They correspond to $Fe_{76}Mo_8Cu_1B_{15}$ AMA irradiated by 80 keV H^+ ions. It should be noted that the spectral lines of CEMS spectra tower up because of emission character of the detected conversion electrons. For comparison, the CEMS spectrum recorded from the wheel side of the sample irradiated with the fluence of 1×10^{16} H^+/cm^2 is also shown in Figure 1b in red color. Note that spectra recorded from both the air and wheel sides of the ribbons are practically identical.

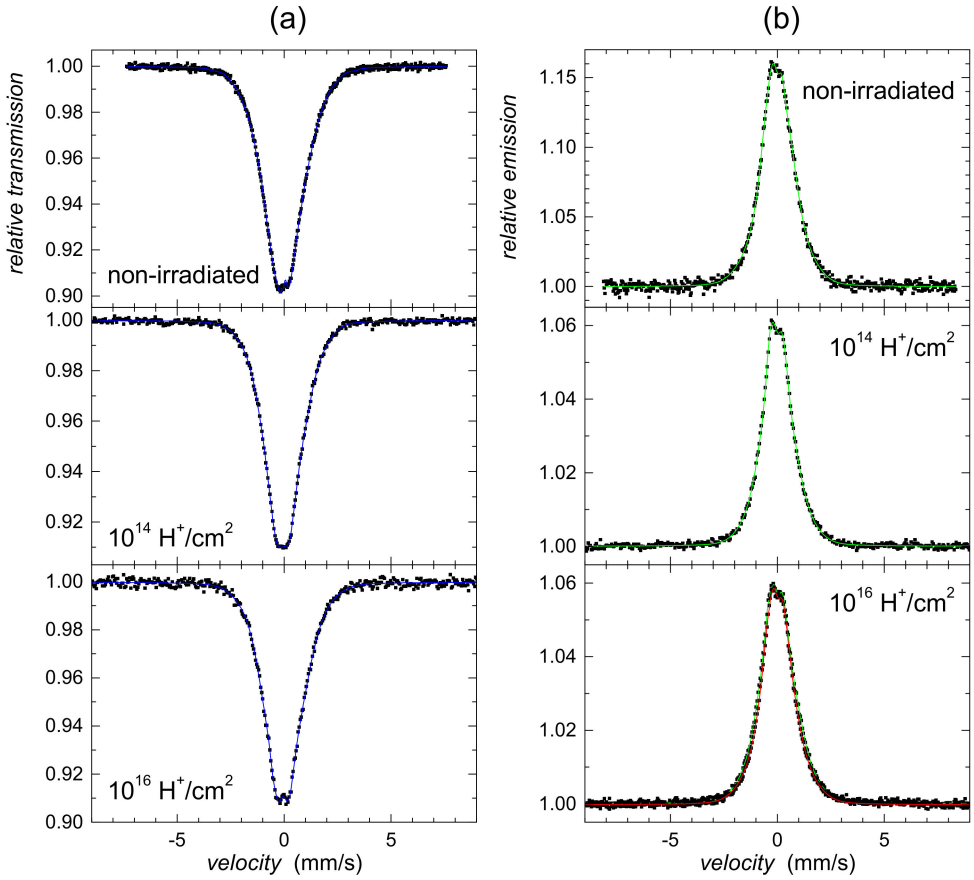

Figure 1. Mössbauer spectra of $Fe_{76}Mo_8Cu_1B_{15}$ amorphous metallic alloy irradiated by 80 keV H^+ ions with the indicated fluences: (**a**) Transmission geometry (blue); (**b**) conversion electron Mössbauer spectroscopy (CEMS, green). Mössbauer spectrum taken from the wheel side of the ribbons is shown for comparison in (**b**) (red).

Both TMS and CEMS spectra show similar line shapes that are characteristic for disordered (amorphous) material which has close-to-room Curie temperature. That is why they consist of regions where magnetic dipole and also electric quadrupole interactions of comparable strength exist. Consequently, $P(B)$ as well as $P(\Delta)$ distributions, respectively, were considered during their evaluation.

The effects of ion irradiation are documented in Figure 2 by evolution of spectral parameters as a function of ion fluence. Here, average values of isomer shift, $\langle\delta\rangle$, and hyperfine magnetic field, $\langle B\rangle$, are plotted as derived from both TMS and CEMS spectra. The contribution of non-magnetic regions—electric quadrupole interactions—was incorporated into the displayed $\langle B\rangle$ values by calculating the weighted average of hyperfine magnetic field and quadrupole splitting expressed in units of Tesla. It should be remembered that ion irradiation took place into the air side of the ribbons. For comparison, the CEMS spectrum of sample irradiated with the ion fluence of 1×10^{16} H^+/cm^2 was collected also from its wheel side. It is almost identical to that from the air side as seen in Figure 1b, its parameters are plotted in Figure 2 by red triangles.

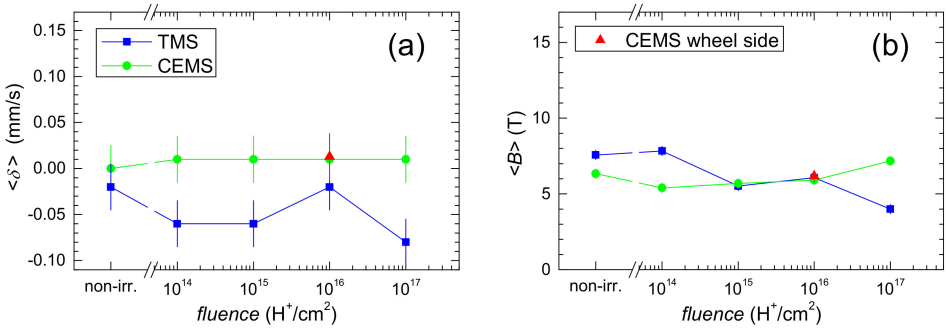

Figure 2. Parameters derived from transmission (TMS, blue) and CEMS (green) Mössbauer spectra of $Fe_{76}Mo_8Cu_1B_{15}$ irradiated by 80 keV H^+ ions plotted against the ion fluence: (**a**) Average isomer shift, $\langle\delta\rangle$; (**b**) average hyperfine magnetic field, $\langle B\rangle$. Red triangles correspond to CEMS spectrum taken from the wheel side of the ribbons. Solid lines are only guides for the eye.

The impact of irradiation by 130 keV N^+ ions on $Fe_{76}Mo_8Cu_1B_{15}$ is shown in Figure 3 using selected TMS and CEMS Mössbauer spectra. Again, the CEMS spectrum of the sample irradiated with the highest ion fluence of 2.5×10^{17} N^+/cm^2 and recorded from its wheel side is provided for comparison in red color.

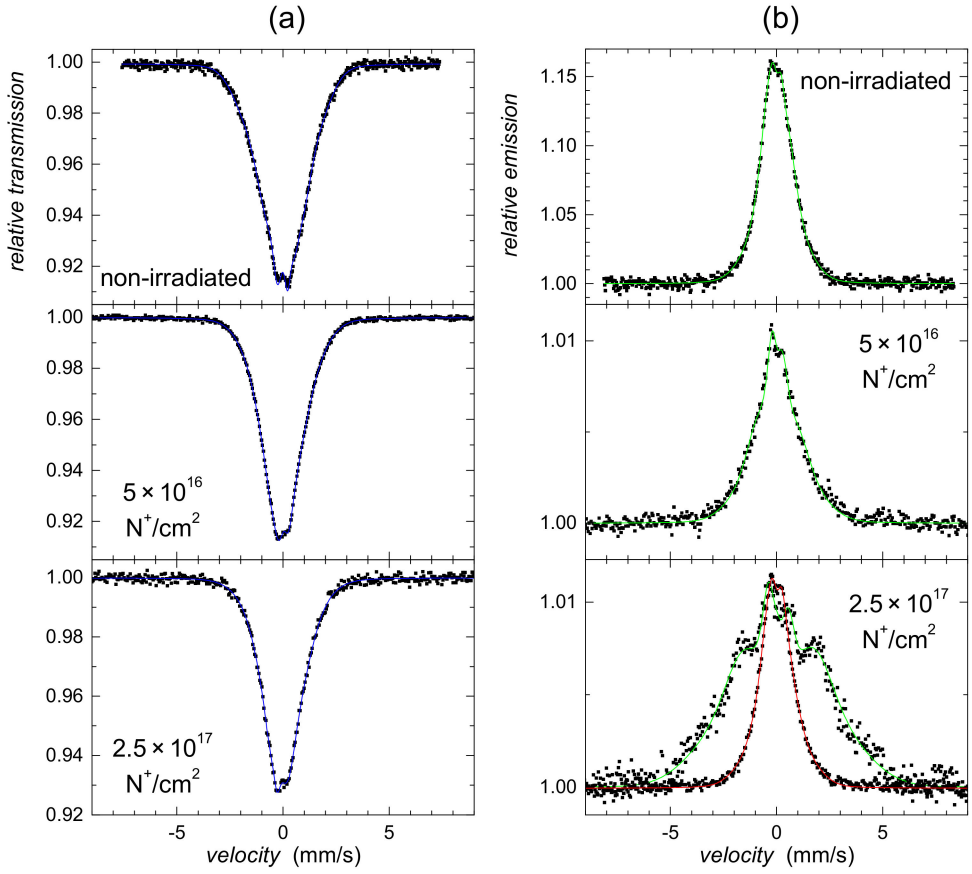

Figure 3. Mössbauer spectra of $Fe_{76}Mo_8Cu_1B_{15}$ amorphous metallic alloy irradiated by 130 keV N^+ ions with the indicated fluences: (**a**) Transmission geometry (blue); (**b**) CEMS (green). The Mössbauer spectrum taken from the wheel side of the ribbons is shown for comparison in (**b**) (red).

The refined principal spectral parameters including $\langle\delta\rangle$ and $\langle B\rangle$ are plotted as a function of ion fluence in Figure 4. Parameters corresponding to the CEMS spectrum recorded from the wheel side of the ribbons are also shown (red tringles). Obvious dissimilarities between the effects of irradiation with H^+ and N^+ ions can be seen. They are highlighted

by the help of differences in the particular parameters in Figure 5. In this way, mutual comparison of changes in the individual spectral parameters that correspond to distinct irradiation modes is possible regardless of their absolute values.

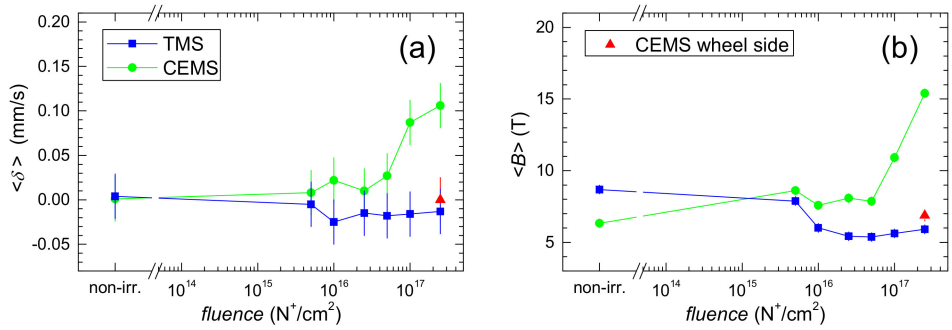

Figure 4. Parameters derived from transmission (TMS, blue) and CEMS (green) Mössbauer spectra of $Fe_{76}Mo_8Cu_1B_{15}$ irradiated by 130 keV N^+ ions plotted against the ion fluence: (**a**) Average isomer shift, $\langle\delta\rangle$; (**b**) average hyperfine magnetic field, $\langle B\rangle$. Red triangles correspond to the CEMS spectrum taken from the wheel side of the ribbons. Solid lines are only guides for the eye.

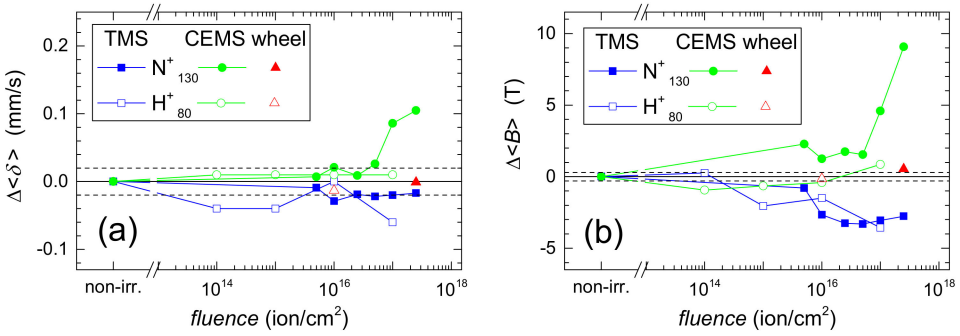

Figure 5. Differences of parameters derived from transmission (TMS, blue) and CEMS (green) Mössbauer spectra of irradiated and non-irradiated $Fe_{76}Mo_8Cu_1B_{15}$ amorphous metallic alloy exposed to 80 keV H^+ and 130 keV N^+ ions as plotted against the ion fluence: (**a**) average isomer shift, $\Delta\langle\delta\rangle$; (**b**) average hyperfine magnetic field, $\Delta\langle B\rangle$. Red triangles correspond to CEMS spectra taken from the wheel side of the ribbons. Solid lines are only guides for the eye, dashed lines represent the error margins.

Differences in average isomer shift, $\Delta\langle\delta\rangle$, and hyperfine magnetic field, $\Delta\langle B\rangle$, were obtained from the values corresponding to irradiated (irr) and non-irradiated (non-irr) samples: $\Delta\langle X\rangle = \langle X_{irr}\rangle - \langle X_{non-irr}\rangle$, where X stands for δ and B, respectively.

3.1.2. FINEMET-Type $Fe_{74}Cu_1Nb_3Si_{16}B_6$ Amorphous Metallic Alloy

The next system, which was irradiated by light ions, is FINEMET-type $Fe_{74}Cu_1Nb_3Si_{16}B_6$ AMA. Protons (H^+) and N^+ ions with the energy of 37 keV and 110 keV, respectively, were used. The mean projected ion penetration range correlates well with the maximum of radiation damage (DPA) and both quantities (see Table 2) fall within the scanning depth of CEMS (~200 nm). Therefore, by choosing appropriate types of ions and their energy, we can control the depth of radiation damage in the particular AMA. To inspect the effects of ion irradiation, both TMS and CEMS techniques were applied. However, contrary to the previous $Fe_{76}Mo_8Cu_1B_{15}$ system, this AMA exhibits at room temperature pronounced hyperfine magnetic interactions. Consequently, its Mössbauer spectra consist of reasonably well-defined sextets of broad and overlapped spectral lines. Selected examples of absorption (TMS) and emission (CEMS) spectra are shown in Figure 6 after irradiation by N^+ ions. Similar CEMS spectra were obtained also from samples exposed to ion irradiation by 37 keV protons (H^+ ions).

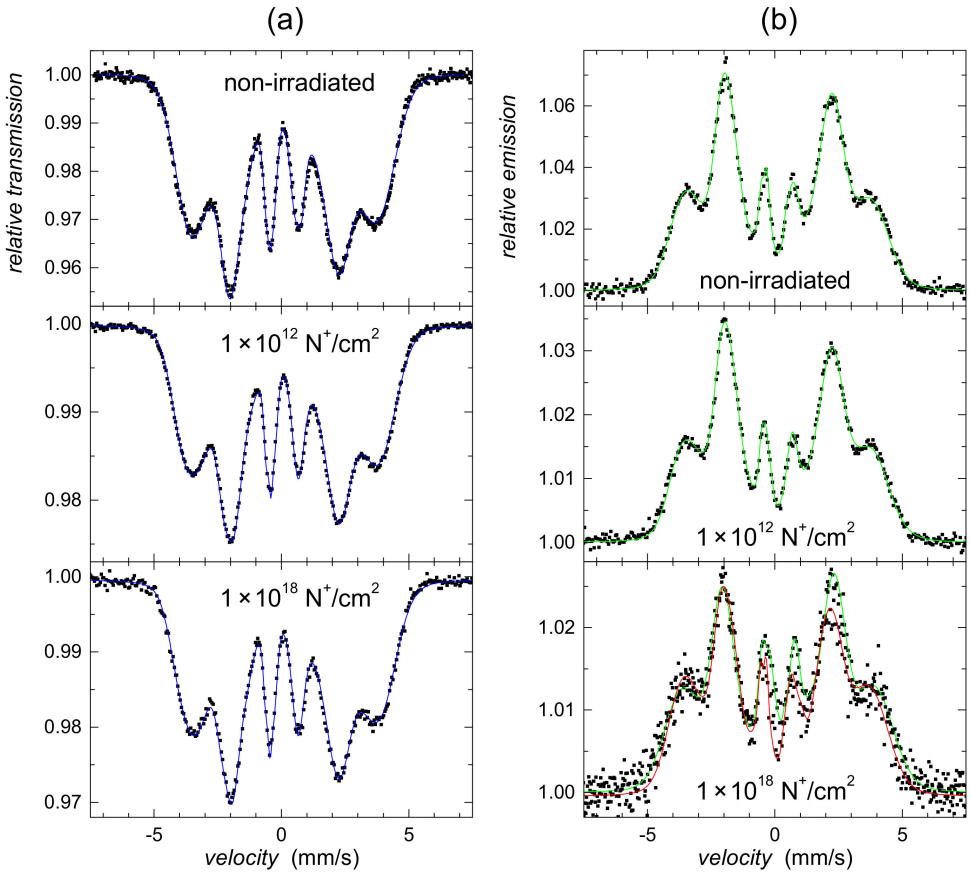

Figure 6. Mössbauer spectra of $Fe_{74}Cu_1Nb_3Si_{16}B_6$ amorphous metallic alloy irradiated by 110 keV N^+ ions with the indicated fluences: (**a**) transmission geometry (blue); (**b**) CEMS (green). Mössbauer spectrum taken from the wheel side of the ribbons is shown for comparison in (**b**) (red).

Values of average isomer shift, $\langle\delta\rangle$, as well as hyperfine magnetic field, $\langle B\rangle$, are plotted as a function of ion fluence in Figure 7. TMS experiments exhibit only minor effects of ion irradiation. Comparison of both irradiation modes—by H^+ and N^+ ions—is again provided by the help of differences in the particular investigated parameters in Figure 8.

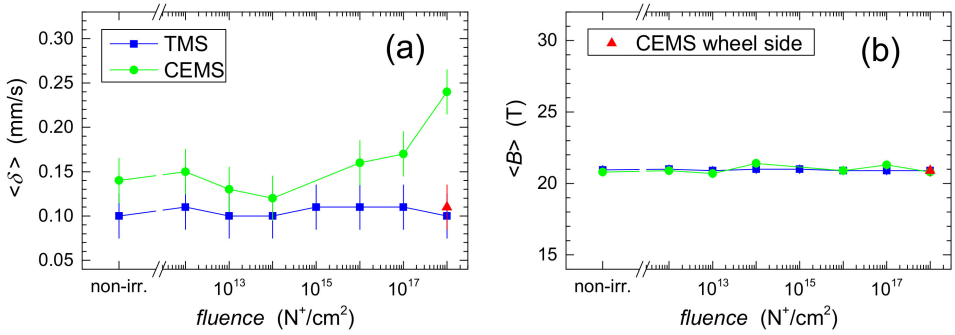

Figure 7. Parameters derived from transmission (TMS, blue) and CEMS (green) Mössbauer spectra of $Fe_{74}Cu_1Nb_3Si_{16}B_6$ irradiated by 110 keV N^+ ions plotted against the ion fluence: (**a**) average isomer shift, $\langle\delta\rangle$; (**b**) average hyperfine magnetic field, $\langle B\rangle$. Red triangles correspond to CEMS spectrum taken from the wheel side of the ribbons. Solid lines are only guides for the eye.

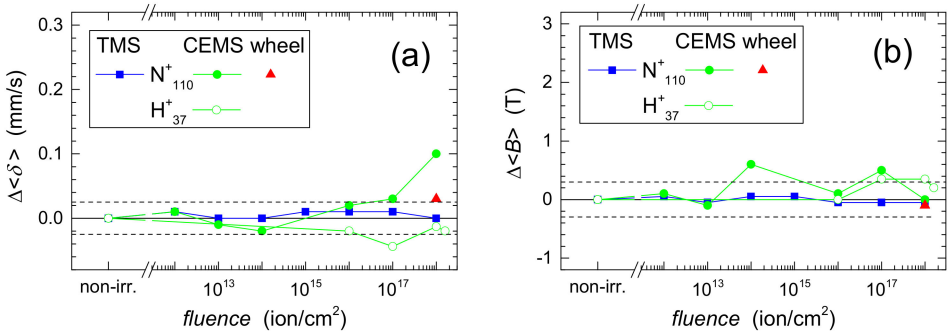

Figure 8. Differences of parameters derived from transmission (TMS, blue) and CEMS (green) Mössbauer spectra of irradiated and non-irradiated $Fe_{74}Cu_1Nb_3Si_{16}B_6$ amorphous metallic alloy exposed to 37 keV H^+ and 110 keV N^+ ions as plotted against the ion fluence: (**a**) average isomer shift, $\Delta\langle\delta\rangle$; (**b**) average hyperfine magnetic field, $\Delta\langle B\rangle$. Red triangles correspond to CEMS spectra taken from the wheel side of the ribbons. Solid lines are only guides for the eye, dashed lines represent the error margins.

It should be noted that we have not performed TMS experiments of H^+-irradiated FINEMET-type AMA because of very low, if any, impact of light ions featuring rather low energy (37 keV) upon this, relatively stable system.

Because the FINEMET-type $Fe_{74}Cu_1Nb_3Si_{16}B_6$ AMA exhibits the presence of ferromagnetic exchange interactions, which are demonstrated by sextuplet Mössbauer line patterns, it is possible to determine orientation of the net magnetic moment of this alloy. This is accomplished via the so-called angle Θ which can be directly obtained from the spectral line intensities [40]. Angle Θ can be derived from the expression $b = (4.\sin^2\Theta)/(1+\cos^2\Theta)$ where b represents relative intensity (area) of the 2nd and/or the 5th spectral line with respect to the 1st, 6th and the 3rd, 4th lines (I_1:I_2:I_3:I_4:I_5:I_6 = 3:b:1:1:b:3). It is an angle between the vector of net magnetization of the sample (absorber) and the propagation direction of γ-rays of a Mössbauer source. It can vary between 0° and 90° which correspond to perpendicular and in-plane orientation of atomic spins, respectively, with respect to the sample. Random orientation of spins—in a powder-like sample—is characterized by Θ = 54.7°, the so-called magic angle. Results of this analysis are shown in Figure 9, where also Θ = 54.7° and Θ = 90° are indicated by horizontal lines.

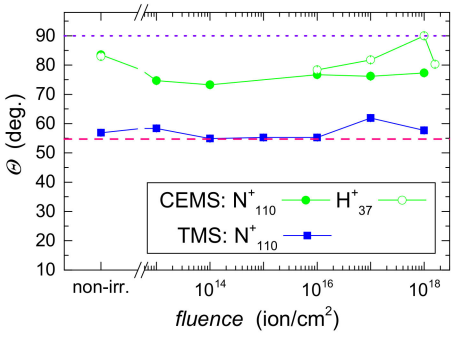

Figure 9. Orientations of net magnetic moments characterized by the angle Θ of the $Fe_{74}Cu_1Nb_3Si_{16}B_6$ amorphous metallic alloy exposed to 37 keV H^+ and 110 keV N^+ ions plotted against the ion fluence. Pink dashed and violet dotted lines represent Θ-values that correspond to random and in-plane orientations of spins, respectively. Solid lines are only guides to an eye.

3.1.3. NANOPERM-Type versus FINEMET-Type Amorphous Metallic Alloy

For the sake of the successive discussion, in this section the radiation effects of light ions upon NANOPERM- and FINEMET-type AMA are mutually compared by differences

in the corresponding spectral parameters. They were extracted from Figures 5 and 8 and plotted together with respect to the particular type of irradiating ions.

Differences in spectral parameters obtained from the evaluation of TMS and CEMS spectra of NANOPERM- and FINEMET-type AMAs irradiated by 80 keV and 37 keV H^+ ions, respectively, are demonstrated in Figure 10. In the case of FINEMET exposed to 37 keV H^+ ions almost no changes in the respective parameters are revealed within the experimental error range as a function of ion fluence.

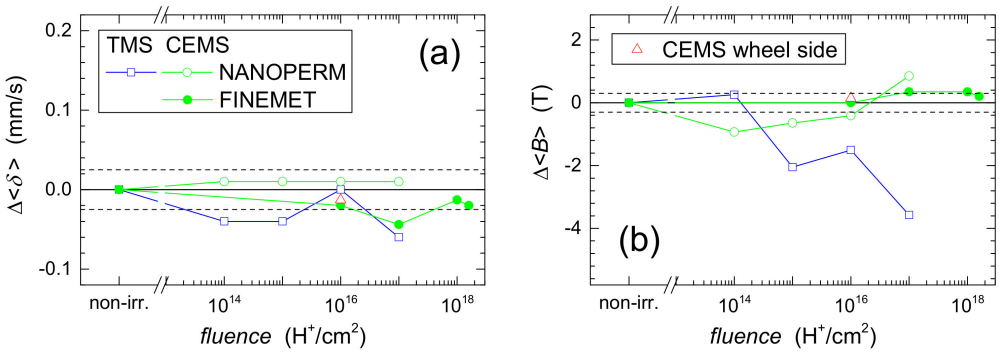

Figure 10. Differences of parameters derived from transmission (TMS, blue) and CEMS (green) Mössbauer spectra of $Fe_{74}Cu_1Nb_3Si_{16}B_6$ (FINEMET-type, solid symbols) and $Fe_{76}Mo_8Cu_1B_{15}$ (NANOPERM-type, open symbols) metallic alloys irradiated by 37 keV and 80 keV H^+ ions, respectively, plotted against the ion fluence: (**a**) average isomer shift, $\Delta\langle\delta\rangle$; (**b**) average hyperfine magnetic field, $\Delta\langle B\rangle$. Red triangles correspond to CEMS spectra taken from the wheel side of the ribbons. Solid lines are only guides for the eye, dashed lines represent the error margins.

Effects of irradiation by N^+ ions upon these two AMAs are illustrated in Figure 11. Again, only negligible impact upon average hyperfine field of FINEMET is observed.

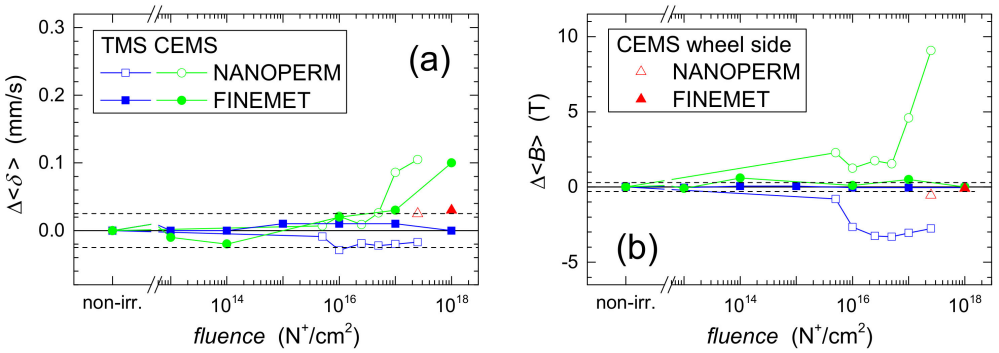

Figure 11. Differences of parameters derived from transmission (TMS, blue) and CEMS (green) Mössbauer spectra of $Fe_{74}Cu_1Nb_3Si_{16}B_6$ (FINEMET-type, solid symbols) and $Fe_{76}Mo_8Cu_1B_{15}$ (NANOPERM-type, open symbols) metallic alloys irradiated by 110 keV and 130 keV N^+ ions, respectively, plotted against the ion fluence: (**a**) average isomer shift, $\Delta\langle\delta\rangle$; (**b**) average hyperfine magnetic field, $\Delta\langle B\rangle$. Red triangles correspond to CEMS spectra taken from the wheel side of the ribbons. Solid lines are only guides for the eye, dashed lines represent the error margins.

3.1.4. $^{57}Fe_{81}Mo_8Cu_1B_{10}$ Amorphous Metallic Alloy

To assess the effects of ion irradiation in more detail, samples enriched by an isotope of ^{57}Fe were prepared. Intentionally, we have chosen NANOPERM-type compositions that are, according to the results presented above and also in [40], more prone to even minor structural modifications. Samples of $^{57}Fe_{75}Mo_8Cu_1B_{16}$ and $^{57}Fe_{81}Mo_8Cu_1B_{10}$ were exposed to N^+ ion beams with the energy of 130 keV which were expected to produce higher radiation damage than the H^+ ones. It is noteworthy that the mean projected range

of N^+ ions is of about 150 nm (Table 2) which matches with the inspection depth of the CEMS technique.

Examples of CEMS spectra taken from both sides of Fe81 ribbons are shown in Figure 12. It should be noted that traces of crystalline phases were revealed even in the as-quenched, i.e., non-irradiated sample on both surfaces. According to the spectral parameters they were recognized as bcc-Fe and Fe_3O_4 (magnetite), the latter being present only on the wheel side [7,39]. These crystalline phases stem from the production process. Their identification was enabled due to higher sensitivity of the CEMS technique which was additionally enhanced by ^{57}Fe enrichment of this sample.

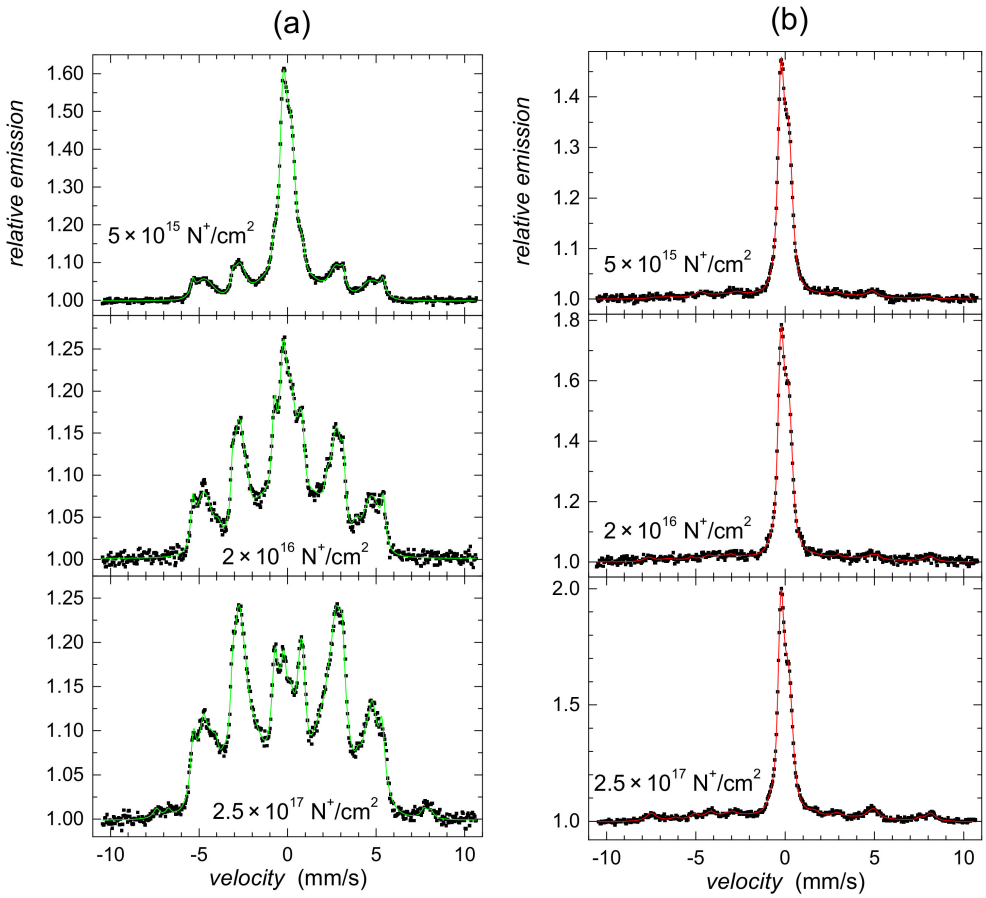

Figure 12. CEMS spectra of $^{57}Fe_{81}Mo_8Cu_1B_{10}$ amorphous metallic ribbons recorded from its: (**a**) Air side (green); (**b**) wheel side (red) after irradiation by 130 keV N^+ ions with the indicated fluences.

After irradiation by N^+ ions, the original doublet-type character of the emission spectra changes dramatically. Sextet-like components appear namely on the air side of the ribbons that was directly bombarded by 130 keV N^+ ions while the wheel side is almost intact.

A detailed view of the evolution of spectral shapes with ion irradiation fluence can be seen in Figure 13 where only the resulting fitted curves are displayed for the sake of clarity and mutual comparison. Note the dramatic decrease in intensity of the central doublet which appears after irradiation with the fluence of 1×10^{16} N^+/cm^2 on the air side.

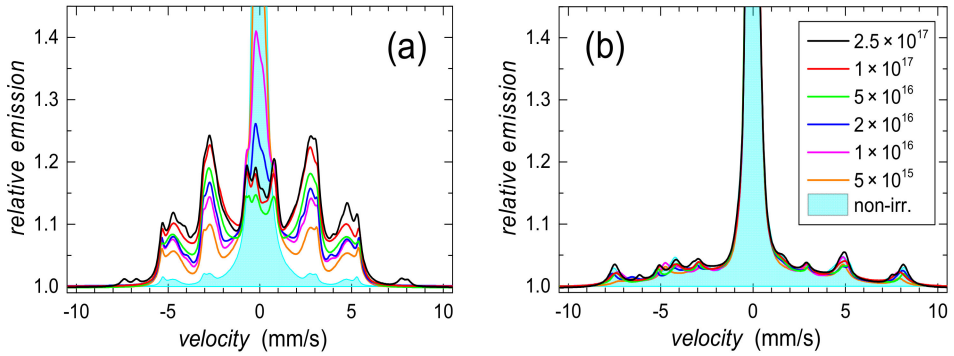

Figure 13. CEMS spectra of $^{57}Fe_{81}Mo_8Cu_1B_{10}$ amorphous metallic ribbons recorded from its: (**a**) air side; (**b**) wheel side after irradiation by 130 keV N^+ ions with the indicated fluences.

Principal spectral parameters comprising average values of isomer shift, $\langle\delta\rangle$, and hyperfine magnetic field, $\langle B\rangle$, corresponding to CEMS spectra from Figure 13, are plotted in Figure 14 as a function of ion fluence.

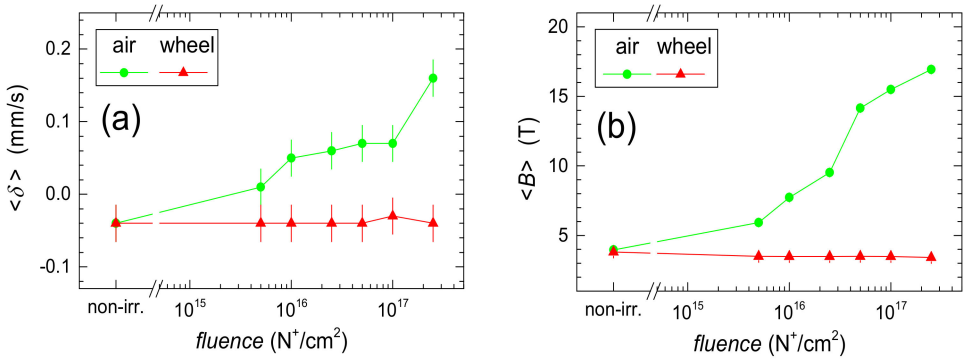

Figure 14. Parameters derived from CEMS spectra recorded from the air (green circles) and wheel (red triangles) sides of the ribbons of $^{57}Fe_{81}Mo_8Cu_1B_{10}$ irradiated by 130 keV N^+ ions plotted against the ion fluence: (**a**) average isomer shift, $\langle\delta\rangle$; (**b**) average hyperfine magnetic field, $\langle B\rangle$. Solid lines are only guides for the eye.

3.1.5. $^{57}Fe_{75}Mo_8Cu_1B_{16}$ Amorphous Metallic Alloy

The effects of N^+ irradiation upon another type of the Fe-Mo-Cu-B system, Fe75, are shown in Figure 15 where CEMS spectra taken from both sides of the ribbons are plotted. Note that the presence of small amounts of magnetite (~7%) was detected only in near-surface regions on the air side which was irradiated to the highest fluence of 2.5×10^{17} N^+/cm^2 as can be seen in Figure 15a.

Deeper regions of this sample that extended down to about 5 μm under the surface were screened by CXMS. Application of this Mössbauer effect technique was enabled due to enrichment of $^{57}Fe_{75}Mo_8Cu_1B_{16}$ AMA in the ^{57}Fe isotope. On the other hand, because of significantly high effective thickness of the enriched AMAs, TMS experiments are not possible as they would provide unreliable data. Selected CXMS spectra obtained from both sides of Fe75 ribbons are shown in Figure 16 and the spectral parameters derived from CEMS and CXMS experiments are collected in Figure 17. Note that no traces of crystalline components are seen in more deep subsurface regions even after irradiation with the highest ion fluence as confirmed by the corresponding CXMS spectrum in Figure 16a.

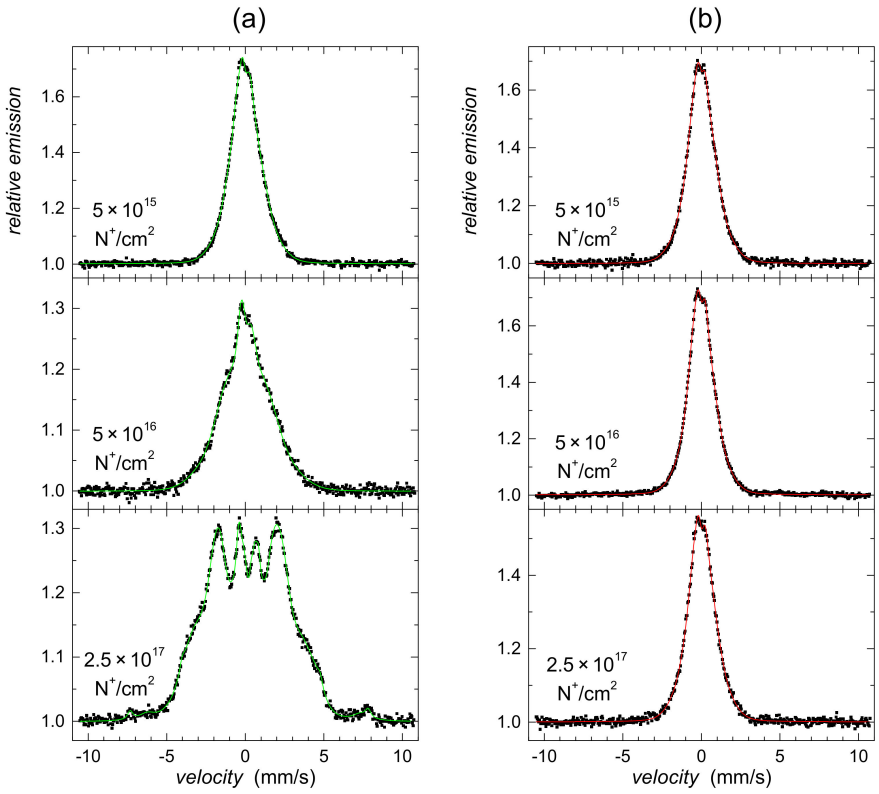

Figure 15. CEMS spectra of $^{57}Fe_{75}Mo_8Cu_1B_{16}$ amorphous metallic ribbons recorded from its: (**a**) air side (green); (**b**) wheel side (red) of the ribbons after irradiation by 130 keV N^+ ions with the indicated fluences.

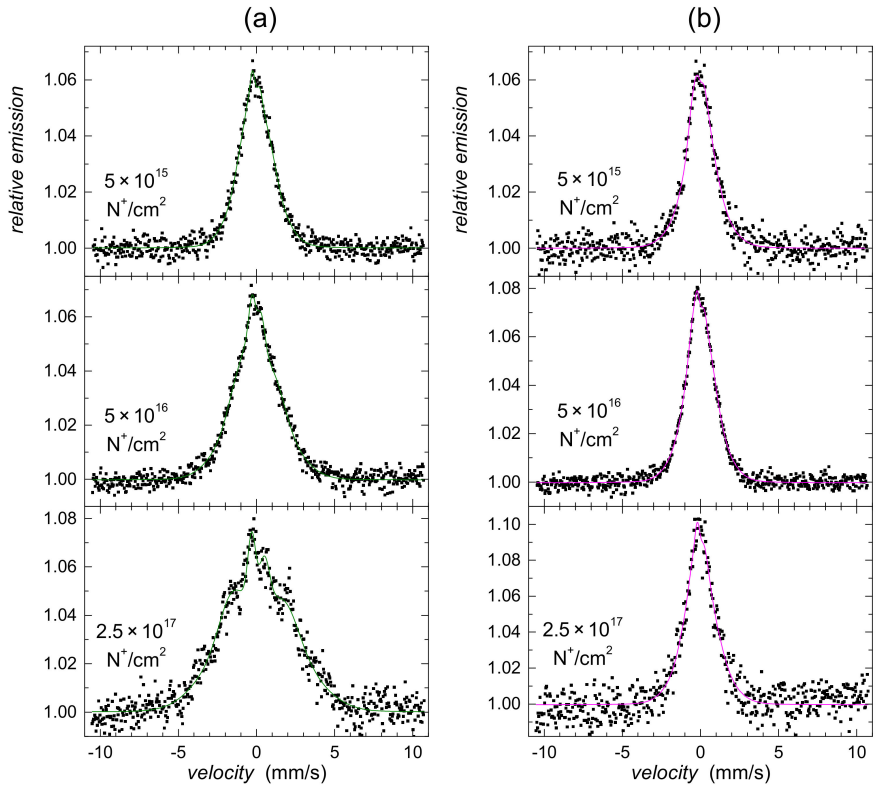

Figure 16. CXMS spectra of $^{57}Fe_{75}Mo_8Cu_1B_{16}$ amorphous metallic ribbons recorded from its: (**a**) air side (dark green); (**b**) wheel side (magenta) of the ribbons after irradiation by 130 keV N^+ ions with the indicated fluences.

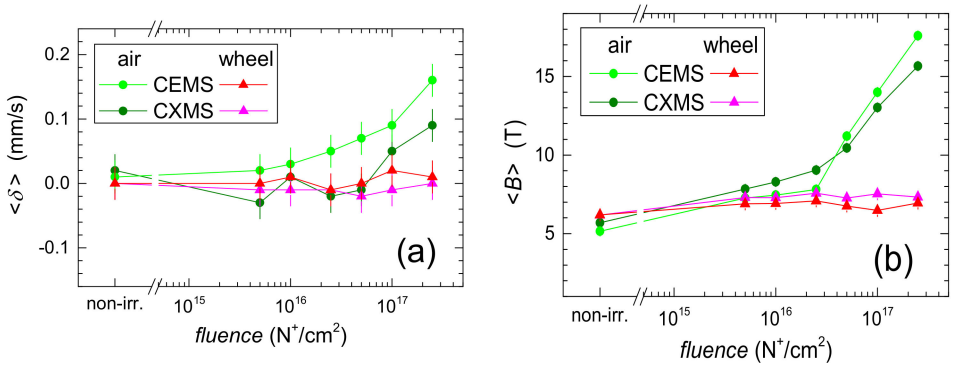

Figure 17. Parameters derived from CEMS and CXMS spectra recorded from the air (circles) and wheel (triangles) sides of $^{57}Fe_{75}Mo_8Cu_1B_{16}$ irradiated by 130 keV N^+ ions plotted against the ion fluence: (**a**) Average isomer shift, $\langle\delta\rangle$; (**b**) average hyperfine magnetic field, $\langle B\rangle$. Solid lines are only guides for the eye.

3.1.6. Fe-Mo-Cu-B-Type Amorphous Metallic Alloys Irradiated by 130 keV N^+ Ions

To summarize the radiation effects of 130 keV N^+ ions upon Fe-Mo-Cu-B-type AMAs, which seem to reflect them more sensitively than the FINEMET-type AMAs, we provide in Figure 18 collective picture of differences in the respective spectral parameters.

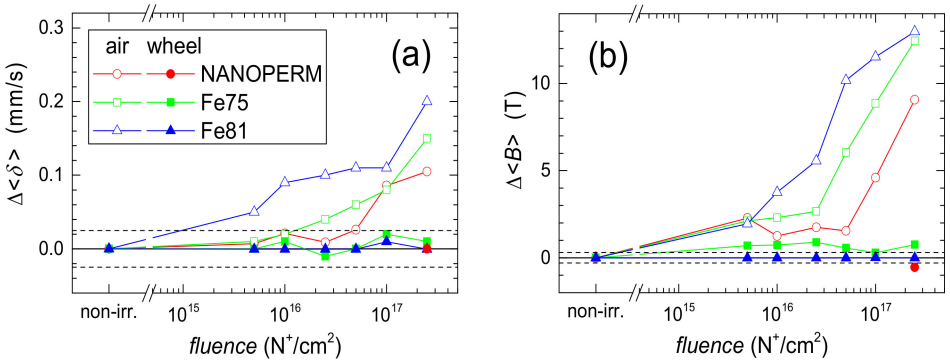

Figure 18. Differences of parameters derived from CEMS spectra of $Fe_{76}Mo_8Cu_1B_{15}$ (NANOPERM-type, red circles), $^{57}Fe_{75}Mo_8Cu_1B_{16}$ (Fe75, green squares), and $^{57}Fe_{81}Mo_8Cu_1B_{10}$ (Fe81, blue triangles) amorphous metallic alloys irradiated by 130 keV N^+ ions plotted against the ion fluence: (**a**) Average isomer shift, $\Delta\langle\delta\rangle$; (**b**) average hyperfine magnetic field, $\Delta\langle B\rangle$. Open and solid symbols correspond to CEMS spectra taken from air and wheel sides of the ribbons, respectively. Solid lines are only guides for the eye, dashed lines represent the error margins.

3.2. Swift Heavy Ions

Swift heavy ions are accelerated to significantly high energies reaching several MeV/u. Consequently, they can penetrate through the whole thickness of the investigated amorphous ribbons (Table 2). Here, we present the results of Mössbauer effect investigations performed upon Fe-Cu-Nb-Si-B-type AMA irradiated by three types of heavy ion featuring also different energies.

3.2.1. VITROPERM $Fe_{73}Cu_1Nb_3Si_{16}B_7$ Amorphous Metallic Alloy

Irradiation of VP 800 was accomplished by ^{238}U, ^{197}Au, and ^{131}Xe ions with the energy of 5.9 MeV/u, 11.1 MeV, and 11.1 MeV/u, correspondingly. Accelerated ions were forwarded towards the air side of ribbon-shaped samples. According to the simulations, the total energy of the ions was so high that they have propagated through the whole thickness of the ribbons (Table 2).

Examples of TMS spectra of VP 800 recorded after irradiation by the particular ions with the indicated fluences are shown in Figure 19, and the corresponding spectral parameters are plotted in Figure 20 as a function of ion fluence.

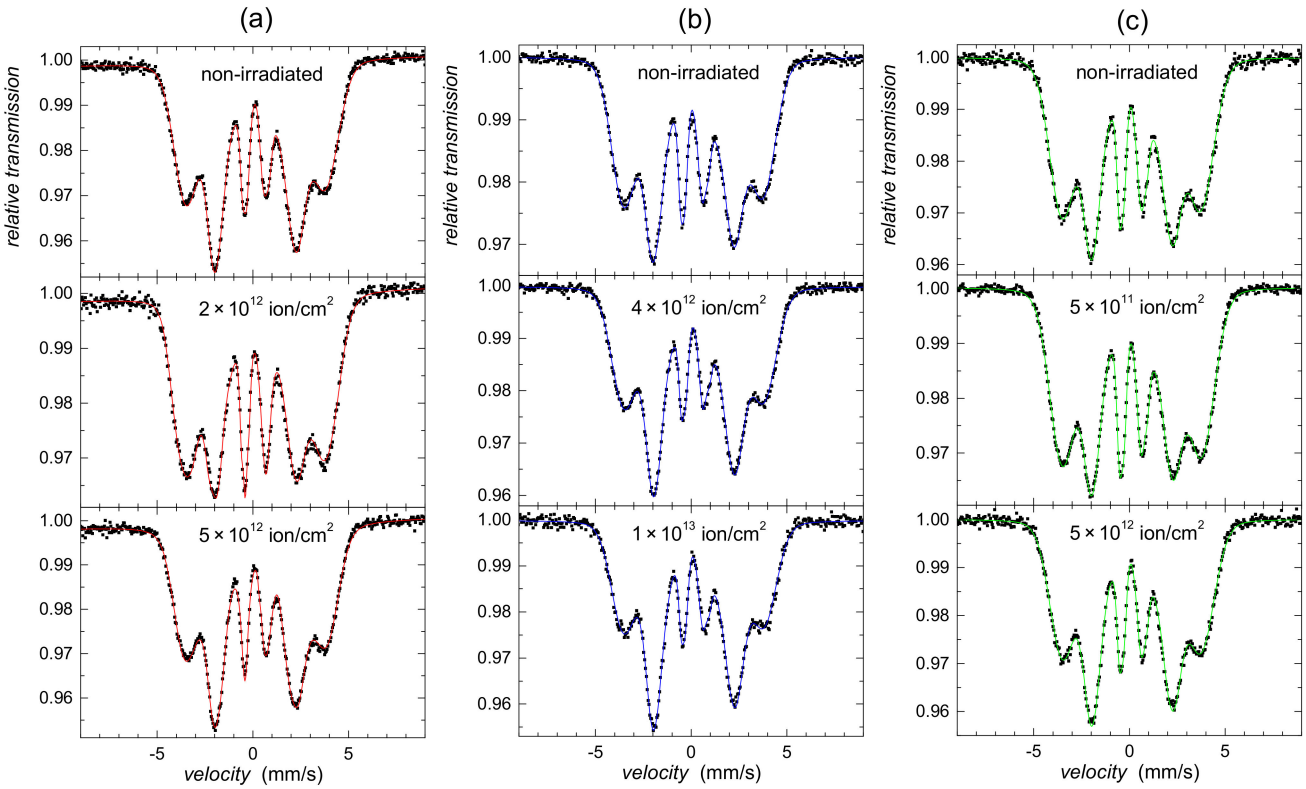

Figure 19. Mössbauer spectra of $Fe_{73}Cu_1Nb_3Si_{16}B_7$ amorphous metallic alloy recorded in transmission geometry after irradiation by: (**a**) 5.9 MeV/u ^{238}U ions (red); (**b**) 11.1 MeV/u ^{131}Xe ions (blue); (**c**) 11.1 MeV/u ^{197}Au ions (green) with the indicated fluences.

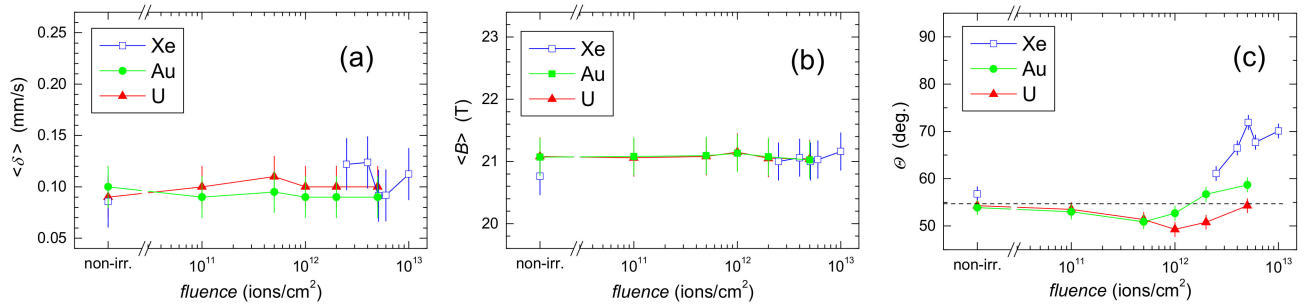

Figure 20. Parameters derived from transmission Mössbauer spectra of $Fe_{73}Cu_1Nb_3Si_{16}B_7$ amorphous metallic alloy irradiated by the indicated heavy ions: (**a**) average isomer shift, $\langle\delta\rangle$; (**b**) average hyperfine magnetic field, $\langle B\rangle$; (**c**) angle Θ as a function of ion fluence. Dashed line in (**c**) represents Θ-values that correspond to random orientations of spins. Solid lines are only guides for the eye.

3.2.2. $Fe_{74}Cu_1Nb_3Si_{16}B_6$ Amorphous Metallic Alloy

FINEMET-type AMA was irradiated by ^{197}Au ions with the energy of 3 MeV/u into the air side of the ribbons. The maximum of the ion penetration range was determined to the depth of 19.3 μm (Table 2) using simulations in a full cascade mode [53]. Taking into consideration the thickness of the ribbon (Table 1), no substantial changes are expected in the corresponding CEMS spectra. Indeed, selected examples of TMS and CEMS spectra in Figure 21 exhibit rather well-defined sextuplet patterns which are characteristic for soft

magnetic AMAs. They were taken from the FINEMET samples exposed to high-energy 593 MeV Au ions with the indicated fluences. Still, CEMS spectra do not show obvious modifications of their shapes and only variations in line intensities can be seen in the TMS spectra.

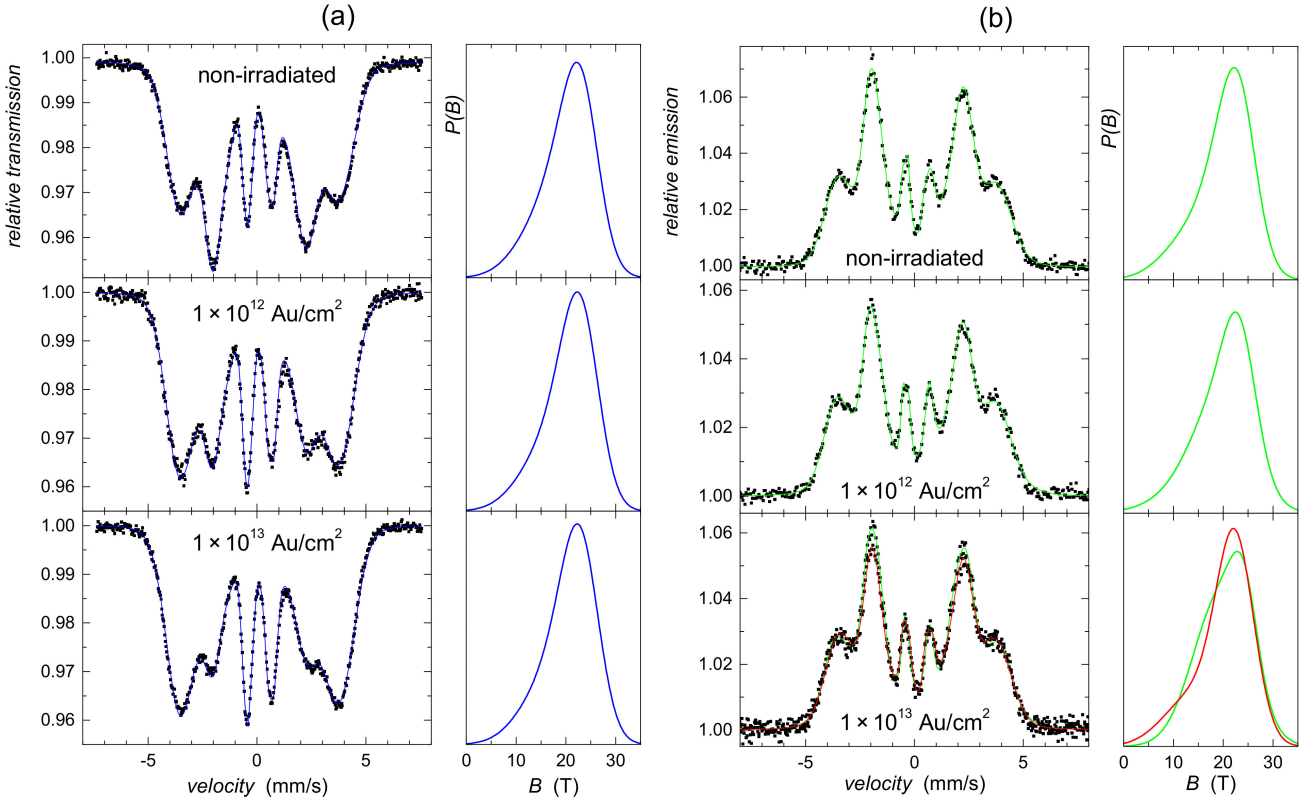

Figure 21. Mössbauer spectra (left-hand panels) and corresponding $P(B)$ distributions (right-hand panels) of $Fe_{74}Cu_1Nb_3Si_{16}B_6$ amorphous metallic alloy irradiated by 593 MeV Au ions with the indicated fluences: (**a**) transmission geometry (blue); (**b**) CEMS (green). Mössbauer spectrum taken from the wheel side of the ribbons is shown for comparison in (**b**) together with the corresponding $P(B)$ (red).

It should be noted that while the total fluences of light ions reached the values of ~10^{18} ion/cm^2, acceleration of heavy ions is experimentally more demanding and that is why the highest fluence is below 10^{13} ion/cm^2.

Spectral parameters derived from the Mössbauer spectra comprising average isomer shift, $\langle\delta\rangle$, average hyperfine magnetic field, $\langle B\rangle$, and angle Θ are plotted against ion fluence in Figure 22. After acquisition of Mössbauer spectra from the irradiated samples, the ribbons were annealed for 1 h in a vacuum at 350 °C with the aim to remove possible radiation damage. Subsequently, TMS experiments were repeated and the obtained spectral parameters are also provided in the figure by solid magenta symbols (1st annealing). Then, a second annealing was performed at the same temperature for 3 h and the corresponding spectral parameters are plotted by open magenta symbols (2nd annealing).

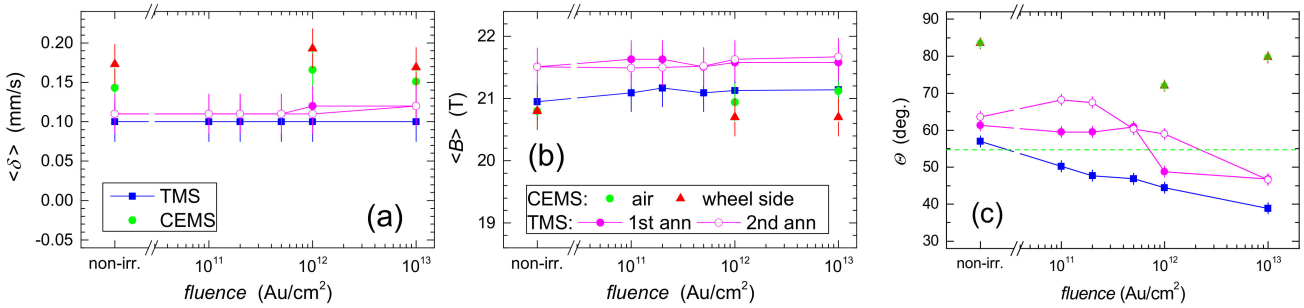

Figure 22. Parameters derived from transmission (TMS, blue) and CEMS (green) Mössbauer spectra of $Fe_{74}Cu_1Nb_3Si_{16}B_6$ irradiated by 593 keV Au ions plotted against the ion fluence: (**a**) average isomer shift, $\langle\delta\rangle$; (**b**) average hyperfine magnetic field, $\langle B\rangle$; (**c**) angle Θ. Red triangles correspond to CEMS spectra taken from the wheel side of the ribbons. Parameters corresponding to the annealed samples are plotted in magenta. Dashed line in (**c**) represents Θ-values that correspond to random orientations of spins. Solid lines are only guides for the eye.

4. Discussion

4.1. Light Ions

Protons, H^+, and nitrogen ions, N^+, were used as representatives of light ions. Simulations performed by the help of the SRIM and S^3M software [53] pointed out that 130 keV N^+ ions produced in NANOPERM almost 100-times higher DPA than 80 keV H^+ ions [54]. Because the maximum penetration depth of the bombarding N^+ ions was ~180 nm and the thickness of the ribbon was ~20 μm, only small irradiation-induced effects were expected in the samples' bulk. As seen in Figure 3a, almost no changes in the spectral lines are revealed in $Fe_{76}Mo_8Cu_1B_{15}$ AMA irradiated by 130 keV N^+ ions. Indeed, the changes in average isomer shift, $\langle\delta\rangle$ derived from TMS, which are shown in Figure 4a, fall within the error range. During TMS experiments, the entire volume of the investigated sample is inspected and that is why the effects of N^+ ions, which are localized in subsurface regions, are not so pronounced.

A higher impact of N^+ ions is documented namely by Mössbauer spectra in Figure 3b where the corresponding CEMS spectra are displayed. Their dramatic broadening is observed with increasing ion fluence. CEMS provides information from surface regions to the depth of ~200 nm which coincides with simulations of the damaged regions (Table 2). That is why considerable deviations in the spectral shapes are observed which are reflected also in the spectral parameters in Figure 4.

A comparison of radiations effects caused by 80 keV H^+ and 130 keV N^+ ions upon $Fe_{76}Mo_8Cu_1B_{15}$ AMA is shown in Figure 5. The higher impact of the latter ions is clearly seen. Consequently, deviations of the spectral parameters provided by CEMS for 80 keV H^+ irradiation are only negligible. Note also that, as in the case of N^+ ions, the wheel side of the irradiated ribbons was again not affected. As far as TMS experiments are concerned, the impact of ion-beam mixing can be seen in both $\langle\delta\rangle$- and $\langle B\rangle$-values. They reflect high sensitivity of this particular AMA to modifications of SRO. Nevertheless, the observed moderate decrease namely in $\langle B\rangle$ is caused by changes of topological SRO. As evidenced by CEMS, however, N^+ irradiation favors the occurrence of magnetic hyperfine interactions due to formation of nitrides in the subsurface regions where majority of N^+ ions is trapped.

With the aim to decrease the penetration depth of protons, we have accelerated them to lower energy of 37 keV during irradiation of FINEMET $Fe_{74}Cu_1Nb_3Si_{16}B_6$ AMA. At the same time, the energy of N^+ ions was also decreased to 110 keV to ensure optimal conditions for CEMS investigations in this AMA (Table 2). As demonstrated in Figure 8, this system is quite resistant to bombardment with the used light ions. Increase of $\langle\delta\rangle$-values after irradiation by N^+ ions is caused by modifications of chemical SRO in the subsurface regions similar as in NANOPERM. Because FINEMET exhibits a pronounced magnetic sextet of Mössbauer lines (Figure 6), orientation of the net magnetic moment was also evaluated. While TMS experiments show almost random alignment of the spins,

CEMS spectra revealed preferential in-plane orientation of the net magnetization as shown in Figure 9.

The effects of light ion irradiation upon NANOPERM and FINEMET are mutually compared by differences in the spectral parameters derived from TMS and CEMS experiments, which can be seen in Figures 10 and 11. Notice the different scales on the y-axes corresponding to $\Delta\langle B\rangle$-values for irradiations by H^+ and N^+ ions.

It is evident that significant radiation effects occur namely in NANOPERM exposed to N^+ bombardment. A notable increase in $\langle\delta\rangle$-values after the fluence of 5×10^{16} N^+/cm^2 is observed. This can be interpreted as modification of the chemical composition (changes in chemical SRO) due to deposition of foreign nitrogen atoms into the original structure. However, no change in isomer shift was revealed at the opposite, i.e., wheel side of the ribbons (red triangles), as expected. This is additional proof that the implanted N^+ ions reside only in spatially confined regions that, moreover, coincide with the inspection depth of CEMS.

As far as average hyperfine fields $\langle B\rangle$ are concerned, a remarkable increase with respect to the original value before ion irradiation is observed from CEMS experiments already after ion bombardment with the smallest fluence of 5×10^{15} N^+/cm^2. Similar to the case of neutron irradiation, this is a consequence of modifications of topological SRO due to atom mixing. TMS results show the opposite trend, i.e., a decrease of $\langle B\rangle$, which, however remains quite stable within the error range for all remaining ion fluences. This behavior can be understood when thermally induced annealing out of the radiation-induced defects is considered. Again, $\langle B\rangle$ derived from CEMS recorded from the wheel side of the ribbons has not changed at all.

The main source of the observed higher radiation damage caused by N^+ ions comes from the higher mass of nitrogen compared to protons. On the other hand, the maximum of 80 keV proton range in NANOPERM is buried quite deeply (~400 nm, Table 2). Consequently, only the plateau-region of the radiation damage profile can be inspected by CEMS and that is why almost no changes are observed in $\langle\delta\rangle$.

Following the aforementioned findings, closer inspection of Fe-Mo-Cu-B (NANOPERM-type) AMAs irradiated by 130 keV N^+ ions was performed using samples with slightly different compositions, namely $^{57}Fe_{81}Mo_8Cu_1B_{10}$ (Fe81) and $^{57}Fe_{75}Mo_8Cu_1B_{16}$ (Fe75). They were, moreover, prepared from iron enriched by isotope ^{57}Fe. Differences of Mössbauer parameters obtained from CEMS and presented in Figure 18 show qualitatively similar features for all three types of the studied NANOPERM-type AMAs. In Fe81, the formation of nanocrystalline bcc-Fe and Fe_3O_4 was revealed already in the non-irradiated sample. After ion irradiation, the presence of nitrides was confirmed by CEMS taken only from the air side of the ribbons and their content was directly related to the ion fluence [39].

Application of CXMS, which provides information from deeper subsurface regions (~5 μm), confirmed the effect of N^+ ions on modifications of chemical SRO which are reflected via $\langle\delta\rangle$-values. As can be seen in Figure 17a, $\langle\delta\rangle$-values are systematically smaller in deeper regions of Fe75 AMA. In other words, higher N^+ fluences are needed to provide comparable radiation damage to that in shallower layers screened by CEMS. It should be stressed that the irradiation depth depends both on the type and energy of the bombarded particles (ions) for the given chemical composition of the AMA. Comparison of Mössbauer spectra in Figures 15a and 16a shows less broadened CXMS lines corresponding to the air side of the ribbons. Again, almost no changes in spectral shapes are observed in the wheel sides.

4.2. Heavy Ions

Radiation effects of heavy ions were investigated on VP 800 and FINEMET AMAs using ions of ^{238}U (5.9 MeV/u), ^{131}Xe (11.1 MeV/u), and ^{197}Au (11.1 MeV/u and 3 MeV/u), with the total fluences of up to 1×10^{13} ion/cm^2. In all cases, with the exception of 593 MeV Au ions (3 MeV/u), the accelerated ions had enough energy to fly through the whole

thickness of the ribbons (Table 2). Consequently, investigations were mainly performed by TMS.

As documented in Figure 20a,b and Figure 22a,b the observed changes in $\langle\delta\rangle$ and $\langle B\rangle$ are negligible regardless of the type and/or energy of the irradiation ions and they fall into the particular error range. This suggests rather high radiation hardness of the studied system. The reason for this can be related to electronic stopping, which attains at the samples' surface the values of 31, 46, and 62 MeV/μm for ^{131}Xe (11.1 MeV), ^{197}Au (11.1 MeV), and ^{238}U (5.9 MeV), respectively. Consequently, unlike in NANOPERM-type AMAs irradiated with light ions, the elastic nuclear scattering is rather small producing $<10^{-3}$ DPA for irradiation by 1×10^{12} U/cm^2 at 5.9 MeV [4]. Thus, radiation damage caused by heavy ions can be probably associated with their high ionization density.

Indeed, the only measurable effect upon Mössbauer spectra in Figures 19 and 21 corresponding to VP 800 and FINEMET, respectively, rests with deviations in the orientation of the net magnetic moment. Quantification of the latter can be derived from the ratio of line intensities (areas) of Mössbauer sextets [40] which are rather well-developed in these soft magnetic AMAs. Even though the spins acquire almost random orientation in the original non-irradiated samples as evidenced by Θ angle in Figure 20c, they tend to rotate out of the ribbon plane after irradiation by ^{197}Au and ^{238}U ions with the fluences of up to 5×10^{11} and 1×10^{12} ion/cm^2, respectively. For higher fluences, spins turn back towards the ribbon plane as observed also after irradiation by ^{131}Xe ions. Therefore, even though no obvious modifications of SRO were observed, rearrangement of magnetic moments takes place as a result of atom mixing.

Considering the results of synchrotron-based X-ray diffraction and X-ray absorption spectroscopy, Michalik et al. [17] suggested that the microscopic origin of changes introduced by swift heavy Xe ions into VP 800 could be similar to those caused by severe plastic deformation and could eventually be removed by appropriate post-irradiation treatment. In fact, this hypothesis can be supported by the results presented in Figure 20c namely for ^{238}U-irradiated VP 800. Even though these ions were accelerated to relatively smaller total energy as compared to the other irradiating ions, due to their high mass they possess the highest electronic stopping at the sample surface [4]. Similar to neutron irradiation [40], collective displacement of atoms takes place also during ion irradiation. Consequently, energy distribution among the atoms, which eventually leads to a local increase in temperature, can be considered. This, in turn, might initiate structural relaxation that is actually governed by the total ion fluence.

Atom mixing after ion irradiation produces elastic stress centers that contribute to the repositioning of magnetic moments of the individual resonant ^{57}Fe nuclei. This results in rotation of the vector of net magnetization out of its original orientation characterized by almost random orientation of the spins towards a slight out-of-plane direction after irradiation with smaller fluences ($<1 \times 10^{12}$ ion/cm^2 in case of ^{238}U). As pointed out by Kuzmann and Spirov [21,55] orientation of spins depends on direction of stresses that occur around defects induced by ion irradiation in the amorphous structure. In-plane compressive stresses acting upon a sample with positive magnetostriction induce an out-of-plane orientation of spins [56] and vice versa. Thus, the way in which the spins tend to rotate with respect to their original position depends on both the sign of magnetostriction of the particular AMA as well as on the nature of stresses present in it (compressive vs. tensile). It should be noted that out-of-plane orientation of spins can be caused also by surface crystallization [57] which can be, eventually, also induced by ion irradiation. After the application of higher fluences, higher energy deposition also takes place which triggers subsequent structural relaxation accompanied by annealing out of stress centers, thus causing rotation of spins in the backward direction, i.e., towards the ribbon plane which is even beyond their original random orientation. This 'additional' rotation of spins is on account of thermally activated structural relaxation. This was confirmed by dedicated experiments the results of which are shown in Figure 22c and discussed in more detail below for the case of FINEMET irradiated by ^{197}Au ions.

From a qualitative point of view, the same phenomenon can be seen in Figure 20c also in the case of VP 800 irradiated by ^{197}Au and ^{131}Xe ions although here "the turning point" of magnetization rotation occurs after irradiation with lower fluences. For ^{197}Au ions it is at 5×10^{11} ion/cm^2 while due to missing data for ^{131}Xe ions this "critical" fluence can be only estimated to be of about the same value. In this respect, we would like to emphasize one important aspect of ion irradiation experiments. Should the irradiation by 5.9 MeV/u ^{238}U ions, i.e., one specific type of ions featuring particular energy, be performed/evaluated only for the non-irradiated AMA and the one exposed to the highest fluence of 5×10^{12} ion/cm^2, the effects of spin rotation caused by ion irradiation might be hindered due to temperature-induced structural relaxation observed at higher fluences. This is demonstrated by almost no change in $\langle\delta\rangle$- and $\langle B\rangle$- as well Θ-values in Figure 20c associated with these end points. Thus, concentrating only on the non-irradiated sample and the highest fluence, the complex radiation effects might be overlooked.

To go even further, let us consider the behavior of net magnetization in FINEMET irradiated by ^{197}Au ions with considerably lower energy (593 MeV) as in the previous experiment with VP 800 (2187 MeV) and/or that of VP 800 irradiated by ^{238}U ions (1404 MeV). Note that the very similar compositions of FINEMET and VITROPERM do not provide significantly distinct environments for the accelerated ions. As seen in Figure 22c, angle Θ continuously decreases over the whole range of the applied fluences. This means, that the original close-to-random orientation of spins in non-irradiated AMA progressively turns out of the plane of the ribbons. The same behavior is observed in Figure 20c, however only over a limited fluence range for VP 800 irradiated by more energetic ^{197}Au ions and slightly broader range for ^{238}U ions. Subsequent increase of Θ-values is supposed to be initiated by thermally-induced structural relaxation as discussed above.

To verify this assumption, FINEMET was thermally annealed for 1 h at 350 °C after irradiation by 593 MeV ^{197}Au ions and acquisition of Mössbauer spectra. In accordance with the data presented in Figure 22c, this first annealing has ensured almost complete recovery of the irradiated microstructure up to the fluence of 5×10^{11} Au/cm^2 and the net magnetic moment has returned to its original position. Nevertheless, structural disordering caused by atom mixing after irradiation with higher fluences was only partially removed and not all radiation defects were annealed out.

Subsequent second annealing for 3 h at the same temperature has caused rearrangement of the spins towards the ribbon plane namely in the samples irradiated with fluences of up to 2×10^{11} Au/cm^2. It is noteworthy that the original non-irradiated specimen is rather stable and no appreciable movement of the spins is observed. On the other hand, prolonged annealing has recovered an additional part of the structure irradiated with the fluence of 1×10^{12} Au/cm^2 which was only partially recovered after the first (shorter) annealing. Still, structural disordering due to ion irradiation with the highest fluence was intact in comparison with the first annealing.

Is should be noted that CEMS spectra taken from both sides of the ribbons exhibit identical values of Θ angles. They were recorded only for some samples and show the same behavior as discussed for VP 800, i.e., a tendency of the net magnetic moment to turn out of the ribbon plane after irradiation with moderate fluences, then return to almost original orientation due to dissipation of thermal energy delivered by the ions with high fluency.

5. Conclusions

In Part I of this paper [40], we have discussed radiation effects in amorphous metallic alloys caused by neutron irradiation as revealed by Mössbauer spectrometry. It was shown that using appropriate chemical composition of the irradiated AMAs, even subtle rearrangements of atoms caused by bombardment with neutrons can be effectively identified. Here, similar phenomena were observed after irradiation with charged particles, namely light and heavy ions. Even though the interaction mechanisms are different their manifestations via Mössbauer spectral parameters are quite similar. This is particularly true as far as swift heavy ions are concerned. Due to their high mass and energy, the induced radiation

damage stays well below 0.1 DPA and that is why it cannot be attributed to elastic nuclear collisions as observed in AMAs irradiated by light ions. Rather, electronic stopping due to their high ionization density should be considered. Thus, the damage caused by swift heavy ions cannot be correlated to DPA. On the other hand, light ions with low ionization density interact predominantly by elastic nuclear collisions which provide approximately 10 DPA in NANOPERM irradiated by N^+ ions with the fluence of 2×10^{16} cm^2 [54].

The achieved results suggest that for light ions with low ionization density, a criterion for tolerable fluence can be based on the radiation damage caused by elastic nuclear collisions. A threshold has been observed (especially for AMAs irradiated by N^+ ions) at the fluence slightly below of 5×10^{15} ion/cm^2 when DPA approaches values of ~8. It is noteworthy that one N^+ ion induces approximately 100 times more vacancies in the peak region compared to one proton. On the other hand, the electronic stopping becomes more important for heavy ions with high ionization density. However, corresponding Mössbauer spectra reflect the effects of irradiation only through reorientations of spins.

Ion irradiation studies were performed under different irradiation conditions comprising several types of irradiating ion, both light and heavy, featuring diverse energies and providing several fluences. In this way, it was possible to unveil even subtle manifestations of rather complex radiation effects in amorphous metallic alloys.

Funding: This research was funded by the Scientific Grant Agency of the Ministry of Education, Science, Research and Sport of the Slovak Republic, grant number VEGA 1/0130/20, by the Slovak Research and Development Agency, grant number APVV-16-0079, and by the European Regional Development Fund-Project "Center for Advanced Applied Sciences", grant number CZ.02.1.01/0.0/0.0/16_019/0000778.

Institutional Review Board Statement: Not applicable.

Informed Consent Statement: Not applicable.

Data Availability Statement: Data supporting the reported results can be obtained from the author upon request.

Acknowledgments: Special thanks are given to P. Švec and D. Janičkovič (Bratislava) for providing samples of amorphous metallic alloys, M. Pavlovič (Bratislava) for fruitful discussions during early stages of this work and M. Cesnek (Prague) for technical assistance with some experiments.

Conflicts of Interest: The author declares no conflict of interest. The funders had no role in the design of the study; in the collection, analyses, or interpretation of data; in the writing of the manuscript, or in the decision to publish the results.

References

1. Spiller, P.; Blasche, K.; Franczak, B.; Kirk, M.; Hulsmann, P.; Omet, C.; Ratschow, S.; Stadlmann, J. Accelerator plans at GSI for plasma physics applications. *Nucl. Instr. Meth. Phys. Res. A* **2005**, *544*, 117–124. [CrossRef]
2. Spiller, P.; Franchetti, G. The FAIR accelerator project at GSI. *Nucl. Instr. Meth. Phys. Res. A* **2006**, *561*, 305–309. [CrossRef]
3. Spiller, P.; Barth, W. FAIR–Status and relevance for heavy ion fusion. *Nucl. Instr. Meth. Phys. Res. A* **2014**, *733*, 171–177. [CrossRef]
4. Pavlovič, M.; Miglierini, M.; Mustafin, E.; Ensinger, W.; Šagátová, A.; Šoka, M. Radiation damage studies of soft magnetic metallic glasses irradiated with high-energy heavy ions. *Rad. Eff. Defects Sol.* **2015**, *170*, 1–6. [CrossRef]
5. Pavlovič, M.; Miglierini, M.; Mustafin, E.; Seidl, T.; Ensinger, W.; Strašík, I.; Šoka, M. Ion irradiation studies of soft metallic glasses. *Acta Phys. Pol. A* **2010**, *118*, 745–755. [CrossRef]
6. Hasiak, M.; Miglierini, M. Magnetic Properties of Ion Irradiated $Fe_{75}Mo_8Cu_1B_{16}$ Metallic Glass. *Acta Phys. Pol. A* **2017**, *131*, 768–770. [CrossRef]
7. Hasiak, M.; Miglierini, M. Impact of ion-irradiation upon microstructure and magnetic properties of NANOPERM-type $Fe_{81}Mo_8Cu_1B_{10}$ metallic glass. *Acta Phys. Pol. A* **2018**, *133*, 680–683. [CrossRef]
8. Wu, Y.; Peng, K. Impact of Ion Bombardment on the Structure and Magnetic Properties of $Fe_{78}Si_{13}B_9$ Amorphous Alloy. *JOM* **2018**, *70*, 861–865. [CrossRef]
9. Peng, K.; Tang, L.; Wu, Y. Evolution of microstructure and magnetic properties of $Fe_{73.5}Si_{13.5}B_9Nb_3Cu_1$ amorphous alloy during ion bombardment process. *J. Magn. Magn. Mater.* **2018**, *460*, 297–301. [CrossRef]
10. Xiaonan Zhang, Y.W.; Mei, X.; Zhang, Q.; Li, X.; Qiang, J. Damage induced by helium ion irradiation in Fe-based metallic glass. *J. Nucl. Mater.* **2017**, *490*, 216–225. [CrossRef]
11. Avasthi, D.K. Some interesting aspects of swift heavy ions in materials science. *Curr. Sci.* **2000**, *78*, 1297–1306.

12. Zhang, K.; Wang, Y.; Zhang, W.; Hu, Z.; Wei, B.; Feng, Y. Crystallization behavior and mechanical response of metallic glass induced by ion irradiation at elevated temperature. *J. Nucl. Mater.* **2021**, *545*, 152618. [CrossRef]
13. Suo, Y.; Zhang, L.; Guan, T.; Mei, X.; Zhang, X.; Zhang, C.; Yang, Y.; Cao, X.; Qiang, J.; Wang, Y. Study on the irradiation damage in Fe-based metallic glasses induced by Ne^{10+} ions. *Fusion. Eng. Des.* **2020**, *157*, 111635. [CrossRef]
14. Luo, Q.; Fan, X.; Miao, B.; Shen, B.; Shen, J. Ar ion irradiation effect on the soft magnetic performance of Fe-based amorphous alloys. *J. Magn. Magn. Mater.* **2020**, *511*, 166962. [CrossRef]
15. Dong, Q.; Yao, Z.; Wang, Q.; Yu, H.; Kirk, M.A.; Daymond, M.R. Precipitate stability in a Zr-2.5Nb-0.5Cu alloy under heavy ion irradiation. *Metals* **2017**, *7*, 287. [CrossRef]
16. Rodríguez, M.D.; Afra, B.; Trautmann, C.; Toulemonde, M.; Bierschenk, T.; Leslie, J. Morphology of swift heavy ion tracks in metallic glasses. *J. Non–Cryst. Solids.* **2012**, *358*, 571–576. [CrossRef]
17. Michalík, Š.; Michalíková, J.; Pavlovič, M.; Sovák, P.; Liermann, H.-P.; Miglierini, M. Structural modifications of swift-ion-bombarded metallic glasses studied by high-energy X-ray synchrotron radiation. *Acta Mater.* **2014**, *80*, 309–316. [CrossRef]
18. Michalík, Š.; Pavlovič, M.; Gamcová, J.; Sovák, P.; Miglierini, M. Effects of Heavy-Ions on Soft-Magnetic Metallic Glasses Studied by Diffraction of Synchrotron Radiation. *Acta Phys. Pol. A* **2017**, *131*, 657–659. [CrossRef]
19. Michalik, Š.; Cesnek, M.; Pavlovič, M.; Miglierini, M. The effects of swift Xe ion bombardment on the amorphous structure of a VITROPERM type alloy. *J. Alloy. Compd.* **2019**, *795*, 69–78. [CrossRef]
20. Vrba, V.; Procházka, V.; Miglierini, M. Identification of spatial magnetic inhomogeneities by nuclear forward scattering of synchrotron radiation. *J. Synch. Rad.* **2019**, *26*, 1310–1315. [CrossRef] [PubMed]
21. Kuzmann, E.; Spirov, I.N. Mössbauer study of amorphous alloys irradiated with energetic heavy ions. *J. Nucl. Mater.* **1985**, *137*, 22–32. [CrossRef]
22. Kuzmann, E.; Lakatos-Varsanyi, M.; Nomura, K.; Ujihira, Y.; Masumoto, T.; Principi, G.; Tosello, C.; Havancsak, K.; Vértes, A. Combination of electrochemical hydrogenation and Mössbauer spectroscopy as a tool to show the radiation effect of energetic heavy ions in Fe–Zr amorphous alloys. *Electrochem. Commun.* **2000**, *2*, 130–134. [CrossRef]
23. Juraszek, J.; Fnidiki, A.; Toulemonde, M. Induced magnetic anisotropy in metallic glasses irradiated by swift heavy ions. *J. Appl. Phys.* **2001**, *89*, 3151–3155. [CrossRef]
24. Kuzmann, E.; Virag, I.; Pöppi, L.; Havancsak, K.; Klencsar, Z.; Novochatskii, I.A.; Garg, V.K.; De Oliviera, A.C.; Vértes, A. Effects of Heavy Ion Irradiation on Short-Range Order of Fe–Cr–P–C Amorphous Alloys Investigated by Mössbauer and DSC Measurements. *Hyperfine Interact.* **2002**, *139/140*, 561–568. [CrossRef]
25. Amrute, K.V.; Kothari, D.C.; Kanjilal, D. Mössbauer study of ferromagnetic metallic glasses irradiated by swift heavy ions at temperatures 100 and 300 K. *Hyperfine Interact.* **2008**, *184*, 599–607. [CrossRef]
26. Stichleutner, S.; Kuzmann, E.; Havancsák, K.; Huhn, A.; El-Sharif, M.R.; Chisholm, C.U.; Doyle, O.; Skuratov, V.; Homonnay, Z.; Vértes, A. Fluence and ion dependence of amorphous iron-phase-formation due to swift heavy ion irradiation in electrodeposited iron thin films. *Rad. Phys. Chem.* **2011**, *80*, 471–474. [CrossRef]
27. Kuzmann, E.; Stichleutner, S.; Sápi, A.; Varga, L.K.; Havancsák, K.; Skuratov, V.; Homonnay, Z.; Vértes, A. Mössbauer study of FINEMET type nanocrystalline ribbons irradiated with swift heavy ions. *Hyperfine Interact.* **2012**, *207*, 73–79. [CrossRef]
28. Stichleutner, S.; Kuzmann, E.; Lak, G.B.; El-Sharif, M.; Chisholm, C.U.; Havancsák, K.; Skuratov, V.A.; Sziráki, L.; Homonnay, Z.; Vértes, A. Effect of swift heavy ion irradiation on the short range order in novel electrodeposited ternary amorphous alloys. *Rad. Phys. Chem.* **2013**, *91*, 166–169. [CrossRef]
29. Sun, J.; Wang, Z.; Wang, Y.; Chang, H.; Song, P.; Shen, T.; Zhu, Y.; Pang, L.; Li, F. Study of local crystallization induced in FeSiNbZrB amorphous alloy by swift heavy ion (SHI) irradiation at room temperature. *Nucl. Instr. Meth. Phys. Res. B.* **2013**, *307*, 486–490. [CrossRef]
30. Kane, S.N.; Shah, M.; Satalkar, M.; Gehlot, K.; Kulriya, P.K.; Avasthi, D.K. Modification of structural and magnetic properties of soft magnetic multi-component metallic glass by 80MeV $^{16}O^{6+}$ ion irradiation. *Nucl. Inst. Met. Phys. Res. B* **2016**, *379*, 242–245. [CrossRef]
31. Luo, Y.; Wang, Z.; Yang, Y.; Dou, Y.; Xie, J.; Peng, H.; Quan, N.; Wu, G.; Yan, W.; Yu, D. Effect of nitrogen ion implantation on phases, crystallization behaviors and magnetic properties of amorphous Fe-Si-B ribbons. *J. Magn. Magn. Mat.* **2019**, *481*, 68–71. [CrossRef]
32. Zhang, X.; Guan, T.; Zhang, L.; Mei, X.; Wang, Y. The influence of successive irradiation of He and H ions on the structure, morphology and property of metallic glass $Fe_{80}B_{13}Si_7$. *Surf. Coat. Techn.* **2020**, *389*, 125609. [CrossRef]
33. Wang, Y.; Zhang, K.; Feng, Y.; Li, Y.; Tang, W.; Zhang, Y.; Wei, B.; Hu, Z. Mechanism of local hardening in metallic glass during He ion irradiation. *Materialia* **2020**, *11*, 100691. [CrossRef]
34. Hou, W.; Mei, X.; Wang, Z.; Wang, Y. Resistance to He^{2+} irradiation damage in metallic glass $Fe_{80}Si_{7.43}B_{12.57}$. *Nucl. Instr. Meth. Phys. Res. B* **2015**, *342*, 221–227. [CrossRef]
35. Zhang, H.; Mei, X.; Wang, Y.; Wang, Z.; Wang, Y. Resistance to H^+ induced irradiation damage in metallic glass $Fe_{80}Si_{7.43}B_{12.57}$. *J. Nucl. Mater.* **2015**, *456*, 344–350. [CrossRef]
36. Miglierini, M.; Lančok, A.; Pavlovič, M. Ion Bombardment of Fe-Based Amorphous Metallic Alloys. *Hyperfine Interact.* **2009**, *189*, 45–52. [CrossRef]
37. Miglierini, M.; Lančok, A.; Pavlovič, M. CEMS studies of structural modifications of metallic glasses by ion bombardment. *Phys. Met. Metall.* **2010**, *109*, 469–474. [CrossRef]

38. Miglierini, M.; Hasiak, M. Impact of ion irradiation upon structure and magnetic properties of NANOPERM-type amorphous and nanocrystalline alloys. *J. Nanomater.* **2015**, *2015*, 175407. [CrossRef]
39. Miglierini, M.; Hasiak, M. Ion irradiation induced structural modifications of $Fe_{81}Mo_8Cu_1B_{10}$ NANOPERM-type alloy. *Phys. Stat. Sol. A* **2016**, *213*, 1138–1144. [CrossRef]
40. Miglierini, M.B. Radiation effects in amorphous metallic alloys as revealed by Mössbauer spectrometry: Part I. Neutron irradiation. *Metals* **2021**, *11*, 845. [CrossRef]
41. Nasu, S. General Introduction to Mössbauer Spectroscopy. In *Mössbauer Spectroscopy, Tutorial Book*; Yoshida, Y., Langouche, G., Eds.; Springer: Berlin/Heidelberg, Germany, 2013; pp. 1–22. [CrossRef]
42. Principi, G. The Mössbauer effect: A romantic scientific page. *Metals* **2020**, *10*, 992. [CrossRef]
43. Gütlich, P.; Bill, E.; Trautwein, A.X. Mössbauer Spectroscopy and Transition Metal. Chemistry. In *Fundamentals and Applications*; Springer: Berlin/Heidelberg, Germany, 2011; pp. 113–118. [CrossRef]
44. Miglierini, M.; Tóth, I.; Seberíni, M.; Illeková, E.; Idzikowski, B. Structure and hyperfine interactions of melt-spun $Fe_{80}Mo_7X_1B_{12}$ (X = Cu or Au) before and after transformation into nanocrystalline states. *J. Phys. Condens. Matter* **2002**, *14*, 1249–1260. [CrossRef]
45. Žák, T.; Jirásková, Y. CONFIT: Mössbauer spectra fitting program. *Surf. Interf. Anal.* **2006**, *38*, 710–714. [CrossRef]
46. Suzuki, K.; Kataoka, N.; Inoue, A.; Makino, A.; Masumoto, T. High saturation magnetization and soft magnetic properties of bcc Fe-Zr-B alloys with ultrafine gain structure. *Mater. Trans. JIM* **1990**, *31*, 743–746. [CrossRef]
47. Yoshizawa, Y.; Oguma, S.; Yamauchi, K. New Fe-based soft magnetic alloys composed of ultrafine grain structure. *J. Appl. Phys.* **1988**, *64*, 6044–6046. [CrossRef]
48. Miglierini, M.; Škorvánek, I. Magnetic Study of Neutron Irradiated FeCrSiB Metallic Glass. *Mater. Sci. Eng. A* **1991**, *147*, 101–106. [CrossRef]
49. Illeková, E.; Janičkovič, D.; Miglierini, M.; Škorvánek, I.; Švec, P. Influence of Fe/B Ratio on Thermodynamic Properties of Amorphous Fe-Mo-Cu-B. *J. Magn. Magn. Mat.* **2006**, *304*, e636–e638. [CrossRef]
50. Pavúk, M.; Miglierini, M.; Vůjtek, M.; Mashlan, M.; Zbořil, R.; Jirásková, Y. AFM and Mössbauer spectrometry investigation of the nanocrystallization process in Fe-Mo-Cu-B rapidly quenched alloy. *J. Phys. Condens. Matter.* **2007**, *19*, 216219. [CrossRef]
51. Kováč, P.; Pavlovič, M.; Dobrovodský, J. A 0.9 MV accelerator for materials research at the STU Bratislava. *Nucl. Instr. Methods Phys. Res. B* **1994**, *85*, 749–751. [CrossRef]
52. Pavlovič, M.; Miglierini, M.; Mustafin, E.; Seidl, T.; Šoka, M.; Ensinger, W. Influence of high energy heavy ions on magnetic susceptibility of soft magnetic metallic glasses. *Acta Phys. Pol. A* **2014**, *126*, 54–55. [CrossRef]
53. Pavlovič, M.; Strašík, I. Supporting routines for the SRIM code. *Nucl. Instr. Methods Phys. Res. B* **2007**, *257*, 601–604. [CrossRef]
54. Mustafin, E.; Seidl, T.; Plotnikov, A.; Strašík, I.; Pavlovič, M.; Miglierini, M.; Stanček, S.; Fertman, A.; Lančok, A. Ion Irradiation Studies of Construction Materials for High-Power Accelerators. *Radiat. Eff. Defects Solids* **2009**, *164*, 460–469. [CrossRef]
55. Kuzmann, E.; Spirov, I.N. Mössbauer study of amorphous alloys irradiated with energetic heavy ions. *Hyperfine Interact.* **1986**, *29*, 1175–1178. [CrossRef]
56. Serfőző, G.; Kiss, L.F.; Daróczi, C.S.; Kisdi-Koszó, É.; Vértesy, G.; Slawska-Waniewska, A. Magnetic measurements of ion-implnated Fe-Cr-Si-B ribbons. *IEEE Trans. Magn.* **1990**, *26*, 1418–1420. [CrossRef]
57. Gupta, A.; Habibi, S.; Lal, S.; Principi, G. Mössbauer study of surface crystallization in metallic glasses. *Hyperfine Interact.* **1990**, *55*, 967–972. [CrossRef]